**KTH Numerical Analysis
and Computer Science**

Colour Scanning Calibration
– a Comparison of Different Methods

Kristoffer Sokolowski

TRITA-NA-E03128

Numerisk analys och datalogi
KTH
100 44 Stockholm

Department of Numerical Analysis
and Computer Science
Royal Institute of Technology
SE-100 44 Stockholm, Sweden

Colour Scanning Calibration
– a Comparison of Different Methods

Kristoffer Sokolowski

TRITA-NA-E03128

Abstract

In this master's project a number of scanner colour calibration methods are evaluated for the purpose of establishing a calibration method for a desktop scanner. A scanner is used when scanning images of homogenous printed areas that subsequently are analysed for the measurement of colour mottle in prints. The master's project has involved studies of several calibration techniques including artificial neural networks using Bayesian learning. The results show that a method based on artificial neural networks using Bayesian learning, and second a method, based on multiple regression of a 20 term polynomial curve fit, yield similar calibration accuracy. The latter calibration method is recommended because it is simpler to implement and requires less computational effort. A mean accuracy of $\Delta E_{ab} < 4$ was achieved in cases when the evaluated printed samples did not show a high amount of gloss variation, implying that the calibrated scanner-acquired images can be considered to fulfil the requirements needed for the colour mottle application purpose. However, when the samples presented a high amount of gloss variation the accuracy did fall, sometimes dramatically, $\Delta E_{ab} > 10$, suggesting that a scanner in this case is a less suitable input device.

Skannerkalibrering – En metodjämförelse

Examensarbete

Sammanfattning

I det här examensarbetet utvärderas en rad olika kalibreringsmetoder med avsikt att finna en metod som kan användas i en bordsskanner. En skanner används för inskanning av homogena tryckta ytor som sedan analyseras för att mäta färgflammighet i tryck. Examensarbetet innefattar studier av flera kalibreringstekniker inklusive artificiella neuronnät som använder Bayesiansk inlärning. Resultaten visar att en metod baserad på artificiella neuronnät med Bayesiansk inlärning, och en annan metod, baserad på kurvanpassning av ett 20 termers polynom, påvisar liknande noggrannhet i kalibrering. Den sistnämnda kalibreringsmetoden rekommenderas på grund av att den är enklare att implementera och kräver mindre datorprestanda. En genomsnittlig noggrannhet av $\Delta E_{ab} < 4$ uppnås när provtrycken inte påvisar någon större glansvariation, vilket innebär att de skannade bilderna kan anses uppfylla kraven som ställs i syfte att konstruera ett program som mäter färgflammighet. Om proverna emellertid påvisar en hög glansvariation faller noggrannheten i kalibreringen, ibland dramatiskt, $\Delta E_{ab} > 10$, vilket antyder att en skanner i det här fallet inte lämpar sig att användas som ett inläsningsinstrument.

Acknowledgements

Contents

List of Figures

List of Tables

Chapter 1

Introduction

1.1 Background

Print mottle or reflectance in inhomogeneities in the print is perhaps one of the most significant aspects of print quality, or rather non-quality to be precise. Today there exist well known methods, based on image processing, for evaluating print mottle in monochrome prints, see [13] and [3]. In the existent monochrome methods, the variation of the reflectance is measured. Further, it is desirable to make equivalent measurements in colour prints. In colour prints, grey level reflectance is not the only varying parameter but also the colour hue and colour saturation must be accounted for when developing a measurement method. Both monochromatic print mottle and a new method for measuring colour print mottle may use a flatbed scanner as the input device to obtain grey level or colour readings from the measured print. Before any measurements of grey level or colour can take place, we must be certain that the calibration of the flatbed scanner is accurate. The existent calibration method used by the STFI Mottling Software, measuring grey levels, is accurate for its purpose, but when measuring colour the calibration must be extended with colour coordinates.

High accuracy in the calibration process is demanded since colour print mottle involves measuring the local variations around a point in the (L^*, a^*, b^*) colour space, then a bad calibration would result in a deformation of the colour space, and consequently yielding an incorrect value of the measured colour print mottle.

Many articles have been published in this field and we particularly explore articles [9], [14], [15], [16], [22] and [27], which also are the starting point of this master's project. Hardeberg [9] presents methods for converting device dependent RGB colour coordinates to device independent colour spaces. One of the presented methods, the complex method, involving a pre-processing step with a cubic root and subsequent calibration using multiple regression of a 20 term polynomial, shows promising results that can be applied on our problem, see Section 1.2. Kang [14] has thoroughly shown how to calibrate colour scanners using a two step procedure, where the first step consists of grey balancing RGB values , see Section 3.3, and

the second step entails calibration using polynomial regression. Kang has also summarized most of the existent calibration techniques in [15], where he also explains the advantages and disadvantages with each of them. Part of the work carried out in [22] consist of taking a closer look on what physical characteristics that exist in a typical flatbed desktop scanner. This is useful information to us, since we must avoid demanding an accuracy that is not achievable because of the physical limitations in the scanner. An artificial neural network approach of colour scanner calibration is made by Vrhel and Trusell in [27] and by Kang and Andersson in [16].

1.2 Problem statement

The main purpose is to propose a calibration method, for a flatbed scanner of today, that will have an accuracy of $\Delta E < 5$. ΔE is the error difference between the correct and calibrated value measured as an Euclidean distance in the target colour space, which in this case is the CIE (L^*, a^*, b^*) colour space, see Sections 2.1.2 and 2.2. The proposed calibration method should yield adequate precision when scanning prints on substrates that are different from the IT8 photographs [1], in this case e.g. printed *full tone* colours patches.

In this master's project we attempt to show much better generalization capabilities, than [16], of neural networks. This is accomplished by using Bayesian learning when training the feed forward neural network, see [5]. The results presented in [27], do not include any generalization capabilities.

Further, we explore and evaluate the results of the research in calibration techniques and finally attempt to propose a calibration method that will achieve the desired accuracy. The proposed calibration is aimed to be used in the present research in developing a method for measuring colour print mottle at Swedish Pulp and Paper Research Institute, STFI.

Chapter 2

Theory

2.1 Colour vision

2.1.1 Human visual system

The Human Visual System (HVS) has developed into an advanced apparatus over millions of years of evolution. Despite its complexity, scientists have over the past years made substantial progress in understanding the physiology of the eye and thereby forming a foundation on how to define measurement of colour in an independent way. This chapter begins with a physiological overview of the HVS, followed by an exploration of the relationship between the HVS and the definition of physical colour measurement.

First, the meaning of "colour", in e.g. perceived colour, colour stimulus or chromatic illumination, must be clarified depending on the circumstances under which it is used. The first term refers to our everyday experience of coloured objects, which involves a phenomenon known as *colour constancy*. Colour constancy explains our ability to perceive the same colour under different illumination conditions. For example, the illumination on a bright sunny day is about 1000 times stronger than indoors, but we still perceive the same colours. The next term, colour stimulus, defines a reference object with a known colour that is used as input in visual experiments. The last term, monochromatic illumination, refers to light sources that emit light with a fixed wavelength, e.g. Helium-Neon laser emits light at 632.8 nm, which we perceive as a red colour.

The visual system detects electromagnetic radiation with wavelengths between 400 and 700 nm, see Figure 2.1, which makes up visible light. The light enters the eye via the Cornea, passing through the Lens and is detected by photoreceptors in the Retina, see Figure 2.2. The photoreceptors are located in the first layer of the Retina and are of two distinct types: rods or cones.

Rods have a peak spectral sensitivity at approximately 510 nm and respond to monochromatic light. There exists around 120 million rods per retina, compared with the smaller amount of cones, approximately 7 million per retina. Rods are extremely sensitive to light, which make them suitable for vision at very low light
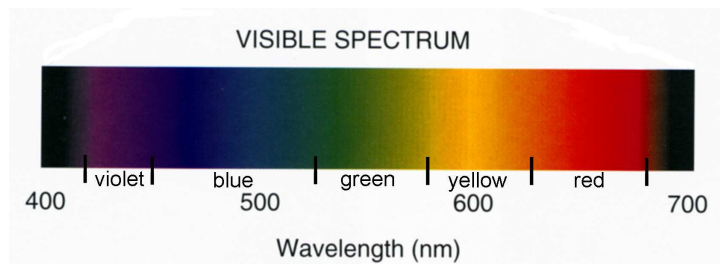
Figure 2.1. The electro magnetic spectrum of visible light.

levels. This is called *scotopic vision*. The rods are located everywhere in the retina except at its centre, the fovea, see Figure 2.2. The image of the surrounding environment we focus on is projected onto the fovea. This constitutes however only about 2 degrees of the visual field. In the fovea, there exists only densely packed cones. They are responsible for our visual experiences under normal lighting conditions, *photopic vision*, and for the perception of colour.
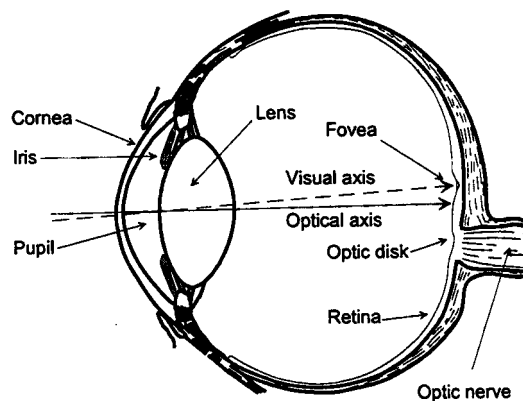
Figure 2.2. A horizontal cross section of the eye seen from above. (From [25] courtesy of Rydefalk.)

When the illumination level gradually changes from higher to lower conditions, i.e. from photopic to scotopic vision, both cones and rods make significant contributions to the visual response in the so called *mesopic vision* form of vision [12]. Rods are more sensitive to shorter wavelengths than cones. An example of this phenomenon and the activation of mesopic vision is that red flowers that appear lighter than blue flowers during daylight, will have the opposite appearance at the end of day. This is also known as the *Purkinje phenomenon*.

Scientists have through indirect methods [12] shown the existences of three types of cones: ρ, γ and β. The notations R, G and B or L, M, and S are also sometimes

4

used. Each type is sensitive to different wavelengths, where ρ corresponds to the sensitivity of the yellow-orange part of the spectrum, γ to the green part and β to the blue-violet part. The different cones are randomly distributed along the retina. The relative proportion between the ρ, γ and β cones are 40 to 20 to 1. These asymmetrical ratios depend on the fact that the eye can hardly correct for chromatic aberration, i.e. the lens acts like a prism where light of different wavelengths hits the retina in various places. The ρ and γ cones are most sensitive at wavelengths of 580 and 540 nm, and β cones are receptive at 440 nm. A consequence of this is that if we focus our eyes on reddish coloured objects with spectral radiation of 560 nm, then surrounding bluish objects will appear blurred.

Different colour sensations are created through either additive or subtractive colour mixture. Additive colour mixture is based on addition of light of different wavelengths. The primary colours red, green and blue are added together to match any colour C. This is governed by Grassman's law of addition [25] $C = R(r) + G(g) + B(b)$, where r, g and b are amounts of the primary colours. In subtractive colour mixture different wavelengths are subtracted or absorbed from the full white light spectrum. Subtractive colour mixture is done in our everyday perception of objects around us. Its most common use is in printing, where the primary colours cyan, magenta and yellow are used as filter of various strengths to produce the desired colour. The additive colours red, green and blue are the opposite colours to the subtractive colours cyan, magenta and yellow. Assume that the (R,G,B) colours are represented as coordinates of equally unit vectors along the x-, y- and z-axis, in a right hand coordinate system, and that the vectors for R, G and B are (1,0,0), (0,1,0) and (0,0,1) with black colour in (0,0,0). Then any additive combination of the (R,G,B) colours will result in an opposite subtractive colour. The added colours can be mentally visualized as the opposite vertices in a cube, where the primary colours are the vertices at the end of the axes. The opposite colour vectors C, M, Y are (0,1,1), (1,0,1), (1,1,0) with the white colour in (1,1,1). Addition of red and green will yield the colour yellow. A thorough mathematical derivation of additive and subtractive colour mixture, using a vector space approach, is presented in [26].

2.1.2 Standard observer

The Commission Internationale de l'Eclarairage (CIE) in year 1931 defined the standard observer. It is an universal standard on how to measure the chromatic illumination of a scene, i.e. the spectral radiation of a coloured object. The standard observer lays the foundation for obtaining device independent colour measurements, e.g. CIEXYZ and CIELAB. These measurements play an important role in this document when calibrating scanners and measuring colour print mottle.

With the standard observer you obtain tristimulus values (R,G,B), which match the eye's spectral response. The tristimulus values should not be confused with (R,G,B) values used in computer graphics or the notations used for different cones. The basis for finding tristimulus values is the use of the colour matching functions, see Figure 2.3.
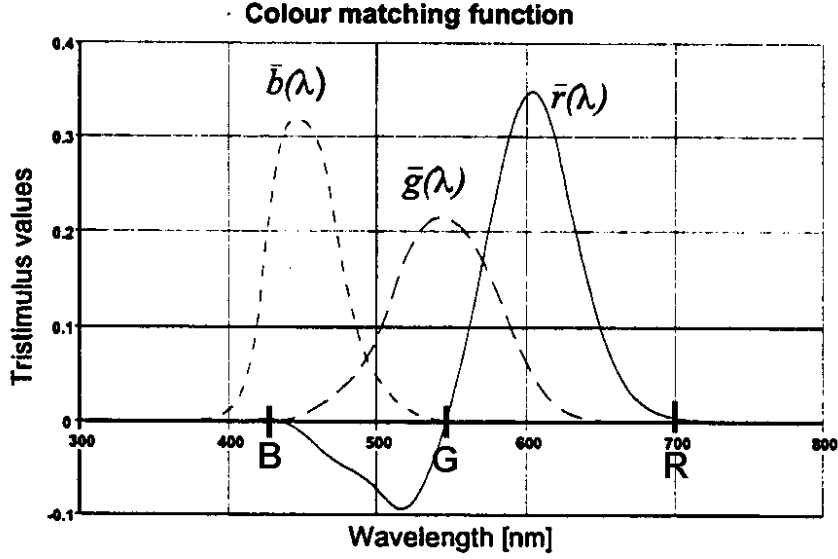
Figure 2.3. The CIE 1931 colour matching functions for $\bar{r}$, $\bar{g}$ and $\bar{b}$ standard 2° observer. (From [25] courtesy of Rydefalk.)

The colour matching function represents the amounts of R, G and B of wavelengths 700.0, 546.1 and 435.8 nm that are added together according to the laws of Grassman, to match a colour stimulus of a certain wavelength. This process is done for the whole visible spectrum, which gives rise to the curves in Figure 2.3. The viewing angle of the standard observer is the angle between the sides of a cone where the top vertex is located in front of the eye and the base area constitutes the observed stimulus. The colour matching function resembles the sensitivities of ρ, γ and β cones shown in Figure 2.4, but are not known with precision to be used as colour matching functions [12]. Calculation of R, G and B values are done with Equation 2.1 where the stimulus spectral power distribution, $\Phi(\lambda)$, is multiplied with a colour matching function.

$$R_1 = \int_{380}^{700} \Phi(\lambda)\bar{r}(\lambda)d\lambda, \quad G_1 = \int_{380}^{700} \Phi(\lambda)\bar{r}(\lambda)d\lambda, \quad B_1 = \int_{380}^{700} \Phi(\lambda)\bar{r}(\lambda)d\lambda \qquad (2.1)$$

The spectral power distribution function $\Phi(\lambda)$ is the sum of reflected, transmitted and absorbed light energy. This unit is measured in amounts of power per small constant-width wavelength interval throughout the visible spectrum.

The tristimulus values (R_1, G_1, B_1) obtained from Equation 2.1 can be seen as a vector in three dimensions, which can be linearly transformed with a 3x3 matrix, A, into another vector: $(R_2, G_2, B_2)^T = A \cdot (R_1, G_1, B_1)^T$. This transformation is only valid when A is linearly independent [17], otherwise there exists no inverse matrix to transform the values back to its original. The same type of transformation can also be done for the colour matching functions, e.g. $(\bar{r_2}, \bar{g_2}, \bar{b_2})^T = A \cdot (\bar{r_1}, \bar{g_1}, \bar{b_1})^T$.
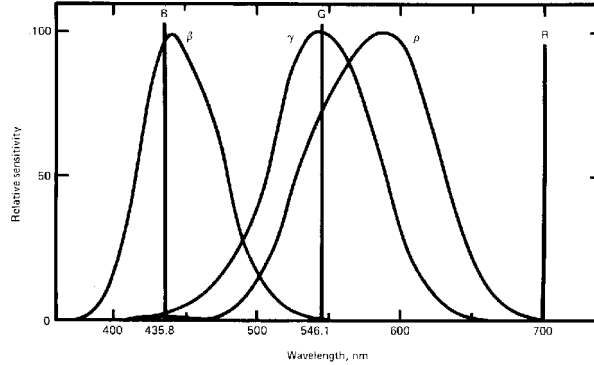
Figure 2.4. The relative sensitivity of ρ, γ and β cones.

These transformations may create tristimulus values that not directly correspond to physical visible values, but have other desirable properties. An example of this is realized by the CIEXYZ 1931 2° observer. The features of the CIEXYZ system are summarized in [25] as:

- All physically realisable colours give positive values (X, Y, Z).

- Achromatic colours give X = Y = Z.

- The ideal white point is represented by X=Y=Z=100.

- The Y-value is proportional to the luminance of the stimulus.

The CIEXYZ system is much more precise than CIERGB, because the surrounding conditions are also specified. Both spectral reflection factor, $R(\lambda)$, of the measured sample and the illumination, $S(\lambda)$, is taken into account when obtaining tristimulus values (X, Y, Z), see Equation 2.2. There are different types of standard illuminants available, see Figure 2.6; a more detailed description of them is found in [4]. All values are normalized with k, see Equation 2.3, and with a perfect reflecting diffuser, $R(\lambda) = 1$, the Y value would have been 100. To only obtain positive tristimulus values, the colour matching functions seen in Figure 2.5 are chosen with no negative parts, compared with Figure 2.3, and are calculated as:

$$
\begin{aligned}
X &= k \int_{\lambda=380}^{700} R(\lambda)S(\lambda)\bar{x}(\lambda)d\lambda, \\
Y &= k \int_{\lambda=380}^{700} R(\lambda)S(\lambda)\bar{y}(\lambda)d\lambda,
\end{aligned}
\tag{2.2}
$$

7

$$Z = k \int_{\lambda=380}^{700} R(\lambda)S(\lambda)\bar{z}(\lambda)d\lambda,$$

$$k = \frac{100}{\int_{\lambda} S(\lambda)\bar{y}(\lambda)d\lambda}. \tag{2.3}$$

Equation 2.2 may also be expressed in discrete form by vector space notation, see details in [28], as defined by Equation 2.4 where $\mathbf{t} = (\text{X,Y,Z})^T$.

$$\mathbf{t} = \mathbf{A}^T \mathbf{L}\, \mathbf{r} \tag{2.4}$$

The $\mathbf{A}$ matrix contains the sampled colour matching functions of size $N \times 3$, where N is the number of samples taken. The spectral reflection of an object is represented by a vector, $\mathbf{r}$, of size $N \times 1$ and the illumination by a diagonal $N \times N$ matrix, $\mathbf{A}$, where the diagonal contains the sampled standard illuminators.

2.2 Colour spaces

The CIEXYZ system does not correspond to the human perception of colour. In other words, a change of colour in CIEXYZ is not perceived with the same proportions by humans. To address the problem, the CIE has defined two new colour spaces, that transform from (X, Y, Z) colour space to the CIE 1976 (L^*, a^*, b^*), and CIE 1976 (L^*, u^*, v^*), colour spaces. In these three-dimensional spaces, the axes, (L^*, a^*, b^*), approximately correlate with perceived lightness, chroma and hue of a stimulus [4]. The most commonly used one in colour printing is CIELAB. CIELUV is sometimes preferred because of its linear relationship with the (X, Y, Z)-space, especially when working with additive colour mixing in television and computer screen applications. Here we only describe the CIELAB and the interested reader can find more information on CIELUV in [4], [12], and [23]. The Equations for L^*, a^* and b^* are as follows:

$$L^* = 116 \cdot f(Y/Y_n) - 16, \tag{2.5}$$

$$a^* = 500\left[f(X/X_n) - f(Y/Y_n)\right], \tag{2.6}$$

$$b^* = 200\left[f(Y/Y_n) - f(Z/Z_n)\right], \tag{2.7}$$

where

$$f(\tau) = \begin{cases} \tau^{1/3} & \text{if } \tau > 0.008856 \\ 7.7867 \cdot \tau + 16/116 & \text{if } \tau \leq 0.008856. \end{cases} \tag{2.8}$$

L^* corresponds to the lightness, where black is represented by 0 units and white by approximately 100 or more units. The a^* and b^* coordinates range from about -100 to +100 units. X_n, Y_n and Z_n correspond to the white object colour stimulus

of the standard illuminant used, see Table 2.1. The difference between a reference stimuli and an estimated stimuli, ΔE_{ab}, e.g. in scanner calibration, is calculated as the Euclidean distance between coordinate points in the (L^*, a^*, b^*) colour space:

$$\Delta E_{ab} = \sqrt{(\Delta L^*)^2 + (\Delta a^*)^2 + (\Delta b^*)^2}. \tag{2.9}$$

In this thesis we treat ΔE_{ab} and ΔE equally. Mean, max and min values are referrred to as ΔE_{mean}, ΔE_{max} and ΔE_{min}.

Table 2.1. The white reference colours for four CIE standard illuminants and two CIE standard observers.

CIE 1931 standard observer (2°)			
Illuminant	X_n	Y_n	Z_n
A	109.850	100	35.585
C	98.074	100	118.232
D50	96.422	100	82.521
D65	95.047	100	108.883
CIE 1964 standard observer (10°)			
Illuminant	X_n	Y_n	Z_n
A	111.144	100	35.200
C	97.285	100	116.145
D50	96.720	100	81.427
D65	94.811	100	107.304

2.3 Scanner calibration

2.3.1 Metamerism

Under certain illumination conditions, we have problems to distinguish between two colour stimuli, even though the stimuli have varying spectral distributions. The samples that cause this phenomena are called *metamers*, see details in [18]. In other words, metamers give rise to the same perceived colour sensation under a given illumination source. Metamers are said to be *metameric* for a given light source and the observer for whom the samples match. If we then change the illumination to another one, which will cause a change in perceived colour; the difference corresponds to the amount of *metamerism*. This physical measurement is referred to as the *CIE metamerism index*, see [18], [25]. When calibrating a scanner there is also a problem with metemeric input, but which is distinguishable by the standard observer. This is due to different spectral sensor sensitivities and is not possible to compensate for when establishing a calibration function. However, the situation could also be the other way around, there could be colours metameric to the standard observer but discernible by the scanner [28]. This is accounted for when determining $\mathcal{F}_{scan}$, see Section 2.3.2.

2.3.2 Definition of scanner calibration

Calibration of a scanner consists of finding the function from the scanner device dependent (R,G,B) space to some device independent colour space, in our case CIEXYZ or CIELAB. This function is often non-linear, especially in the case of RGB to CIELAB mapping where there is a built in the non-linearity due to the cubic root in Equation 2.8.

The mathematical definition of a recording procedure is as follows [28]:

$$\mathbf{z}_i = \mathcal{H}(\mathbf{M}^T \mathbf{r}_i), \qquad (2.10)$$

where z_i is the recorded value at point i in device dependent coordinates, e.g. (R,G,B). Matrix $\mathbf{M}$ is of size $k \times 3$, with k bands of spectral sensitivity including the scanner illuminant, and vector r_i is the spectral reflectance at spatial point i. Vector r_i is of size $k \times 1$, containing k spectral responses. The process of calibrating a scanner is to determine a function $\mathcal{F}_{scan}$ such that:

$$\mathbf{t} = \mathbf{A}^T \mathbf{L} \mathbf{r} = \mathcal{F}_{scan}(\mathbf{z}) \qquad (2.11)$$

for all $\mathbf{r} \in B_{scan}$, where B_{scan} is the range of detectable reflectance spectra of the scanner [28]. The transformation $\mathcal{F}_{scan}$ is created by measuring a set of colour reference patches, e.g. ANSI IT8/7.2 [1], and then finding an appropriate mathematical expression which reflects the relationship between values read by the scanner and values obtained from measurement. Standard regression techniques, e.g. least-squares or singular value decomposition, are then applied [17]. The calibration procedure is mathematically defined as:

$$\mathcal{F}_{scan} = \arg \left(\min_{\mathcal{F}} \sum_{i=1}^{M_q} \|\mathcal{F}(\mathbf{c}_i) - \mathbf{t}_i\|^2 \right), \qquad (2.12)$$

where M_q is the number of patches and $\| \cdot \|^2$ usually is the error metric defined in Equation 2.9. The goal is to achieve such precise calibration, so that error falls within *just noticeable difference*, JND. This means in reality that the perceivable colour difference for two colour samples shown side by side is $\Delta E_{ab} = 2.3$, see [19].
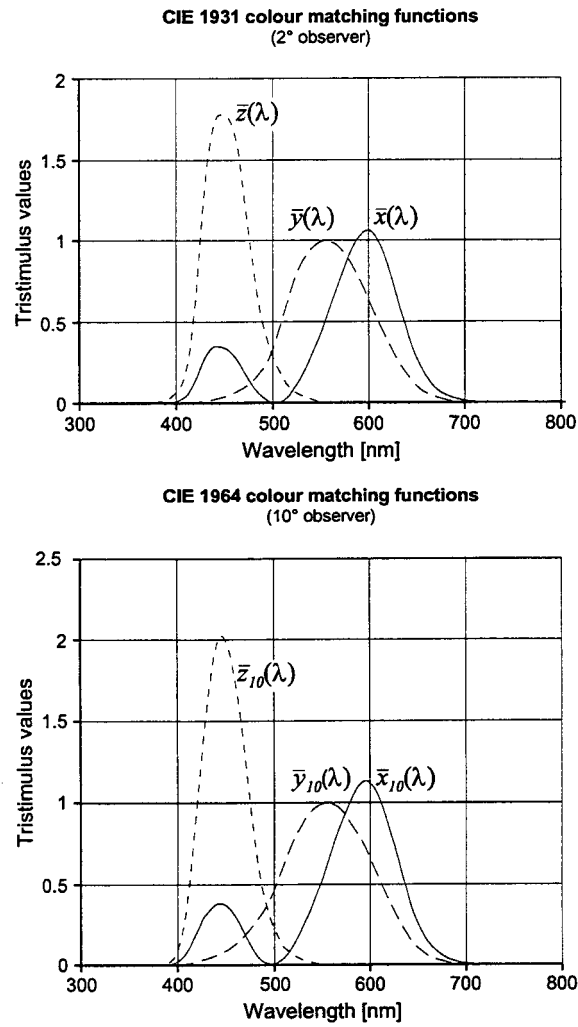
Figure 2.5. The CIEXYZ 1931 2° and CIEXYZ 1964 10° standard observer colour matching functions, $\bar{x}$, $\bar{y}$ and $\bar{z}$. (From [25] courtesy of Rydefalk.)
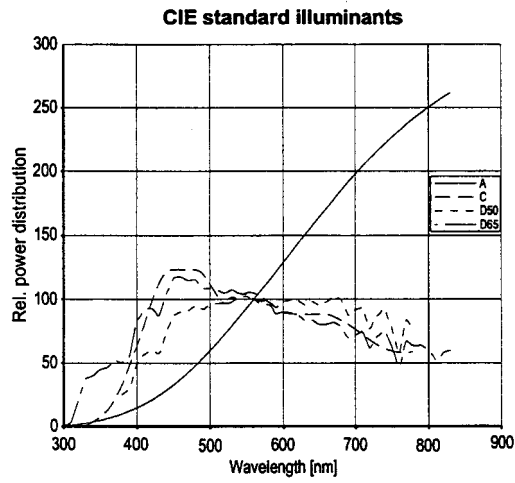
Figure 2.6. The relative power distribution of standard illuminants. (From [25] courtesy of Rydefalk.)
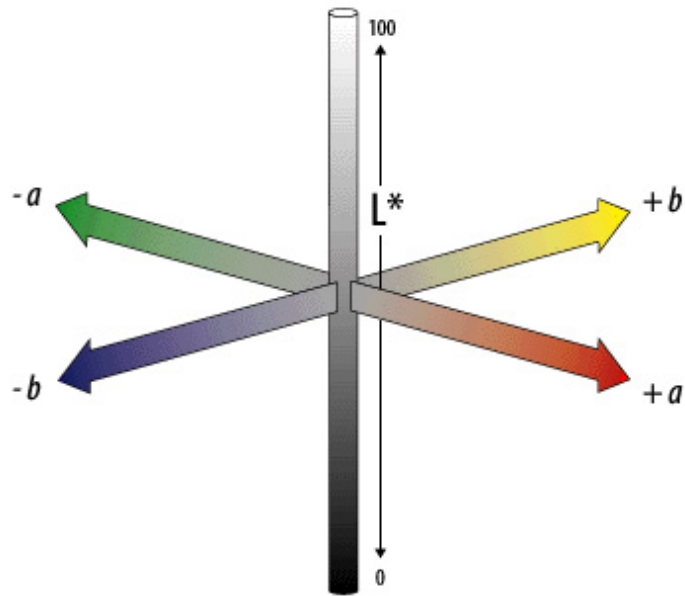
Figure 2.7. The CIELAB coordinate system.

2.4 Colour print mottle

Monochromatic print mottle refers to unevenness in a printed area due to varying reflectance properties in the print, that otherwise should appear uniform. The reason for this may be unevenness in ink transfer in the printing process or optical effects of the ink in the paper. A measure of print mottle, *coefficient of variation of reflectance*, is suggested in [13] as:

$$\mathrm{CV_R} = \mathrm{COV_R} = \frac{\sigma_R}{\overline{\mathrm{R}}}, \tag{2.13}$$

where σ_R is the standard deviation of reflectance and $\overline{\mathrm{R}}$ is the mean value of reflectance. The $\mathrm{COV_R}$ is derived from the law of Weber:

$$k = \frac{\Delta I}{I}, \tag{2.14}$$

which describes the ratio between a change in stimulus, ΔI, and stimulus magnitude, I. The value of k is constant for different stimulus sources, e.g. reflectance in printed paper, $k \approx 0.22$ [13], or perceived luminance level L^*, see Equation 2.5. In other words, print mottle describes spatial variation, or difference of stimulus, in relation to some surrounding average stimulus.

The human visual system is also capable of discriminating between contrast varations of different coarseness in a print [13]. Such type of variations may easily be studied in the frequency domain using Fourier analysis, see [7]. This suggests that a Fourier analysis of (R,G,B)- or (L^*, a^*, b^*)-values could be used to measure print mottle.

The $\mathrm{COV_R}$ may not always apply properly for low values of R, see [6]. Therefore, new models have been studied [3] which involves differentiation of Equation 2.5:

$$\mathrm{d}L^* = c_1 \frac{\mathrm{d}Y}{Y^{2/3}} \tag{2.15}$$

A more general model is also proposed [3]:

$$m = \frac{\sigma}{R^p + c} \tag{2.16}$$

Studies made by Fahlcrantz, Johansson and Åslund [3], suggest that the best correlation between calculated and perceived print mottle is approximately yielded when $p = 1/2$ $(c = 0)$, which gives rise to the following expression for print mottle:

$$m = \frac{\sigma}{\sqrt{R}} \tag{2.17}$$

Print mottle is often studied at different wavelengths by taking the Fourier transform of reflectance levels in the image. The image is typically divided into different bandpasses with ranges in millimetres (0.25, 0.5-1, 1-2, 2-4, 4-8, 8-16), where the best correlation between calculated and perceived print mottle is in the 1-8 mm wavelength bands [13].

Colour print mottle extends the variations in reflectance to include variations in the (L^*, a^*, b^*) space. An expression for colour variations is proposed by Mizes [20] as:

$$m_{cm} = \sqrt{(k_L \, \sigma_L)^2 + (k_a \, \sigma_a)^2 + (k_b \, \sigma_b)^2}, \qquad (2.18)$$

where k_L, k_a and k_b are determined on empirical basis by visual evaluation of print mottle. (the * has been removed in Equation 2.18 for clarity). The fractions between k_L, k_a and k_b are empirically estimated to be about 9:3:1 [20].

Calculation of colour print mottle is carried out by Fourier transformation of each of the components in (L^*, a^*, b^*), and the Fourier responses within the range most detectable by the human visual system, f_{visual}, is added together to give Equations:

$$
\begin{aligned}
\sigma_{L^*} &= \mathcal{F}(L^*)_{f_{visual}} \\
\sigma_{a^*} &= \mathcal{F}(a^*)_{f_{visual}} \\
\sigma_{b^*} &= \mathcal{F}(b^*)_{f_{visual}}.
\end{aligned}
\qquad (2.19)
$$

Chapter 3

Methodology

In this chapter we describe the apparatus, methods and materials that are needed to accomplish the desired goal, see Section 1.2. To find the calibration function in Equation 2.12, reference values are needed to verify the accuracy of the calibration. Therefore, a high accuracy instrument is used for this purpose, see Section 3.1. Then, to test the generalization capabilities of the calibration, the verification material is used, see Section 3.2.1, which also is measured with the same instrument.

When seeking the calibration function, $\mathcal{F}_{scan}$, a number of methods are evaluated. The initial type of calibration method that we want to investigate is a linear calibration function, see Section 3.4.1. The purpose is that we want to find out if $\mathcal{F}_{scan}$ is linear. If that is not the case, we further evaluate more complex methods, a non-linear function, see Section 3.4.3, and an artificial neural network, see Section 3.4.2. The former method has been used before and we want to verify and evaluate the previous results. The latter method, which is completely different from the others described, is evaulated to see if it is a feasilbe calibration method and to verify the results from the non-linear calibration method.

3.1 Apparatus

Reference and verfication values in both (X, Y, Z) and (L^*, a^*, b^*) coordinates are obtained with a high accuracy spectrophotometer "GREGTAG SPM 100-II". The mathematical transformation, (see Equations 2.5, 2.6 and 2.7), from measured (X, Y, Z) values to calculated (L^*, a^*, b^*) values, differs maximally 0.02 units in the L^* axis, 0.15 units in the a^* axis and 0.08 units in the b^* axis, compared with measured (L^*, a^*, b^*) values. All measurements are carried out under illuminant D50 and a $2°$ standard observer. No polarization filters are turned on. The instrument shows good accuracy over months of repetitive measurements of the same absolute white point, $\Delta E < 0.4$.

The recording apparatus used in the calibration process is a typical flat bed scanner "EPSON EXPRESSION 1680 Pro". The scanner's maximum resolution is 1600 dpi, and all the calibration tests are conducted with a resolution of 300 dpi.

The manual does not specify any *colorimetric* accuracy figures, which implies that the scanner is non-colorimetric, i.e. it is not able record values as a standard observer would, see Section 2.1.2. Using a non-colorimetric scanner, we have to assume that it suffers from characteristic flaws [22], i.e. "Boundary effects", "Unsuitable scanner R,G,B sensibilies" and "Neighbourhood influence on scanned pixel values". These flaws may, in the worst case, result in an inherit cumulative error of $5 \leq \Delta E \leq 10$, which can not in a simple way be compensated for in the calibration process.

3.2 Material

3.2.1 Reference material

The reference calibration material used is the industrial standard calibration chart IT8.7/2-1993 [1], see Figure 3.1. It contains 288 (L^*, a^*, b^*) points where some of the values are mandatory according to the IT8 specification and some are defined by the manufacturer of the calibration chart. The mandatory points are evenly spread in middle of (L^*, a^*, b^*) colour *gamut*, while the manufacturer's consist of basic colours (cyan, magenta, yellow, red, green and blue), whose coordinates start in the outer parts of the colour gamut and are continuously evenly spread through the hole gamut. To extend the reference material, 50 additional calibration patches were added. The extra patches are colours defined by the "Natural Colour System" [25], [4], and are shown in Figure 3.2. Both calibration charts have been measured with GREGTAG and saved in ASCII format according to the IT8 specification [1]. When finding the calibration function, combinations of different setups of reference materials are evaluated, i.e. calibration is made with either one or both calibration charts.

3.2.2 Verification material

To verify the accuracy of the calibration, two different printed colour tests was used. The first test, see Figure 3.3, contains 40 samples from a IT8 printed with *halftone* colours. The second test was made up of 8 patches, see Figure 3.4, printed with *full tone* colours on 3 different types of paper with varying gloss properties, consequently, adding up to 24 samples in the batch. The amount of gloss was greatest in the first type of paper, and of decreasing quantities in the others, where the last type of paper showed the least glossiness. The printed tests were measured by the GREGTAG instrument in the same way as the reference calibration material.

Figure 3.1. IT8.7/2-1993.

Figure 3.2. NCS surfaces.

Figure 3.3. Verification of the calibration using 40 samples from a IT8 printed with halftone colours. The white circles marks the outliers in calibration process, see Section 4.1.2.
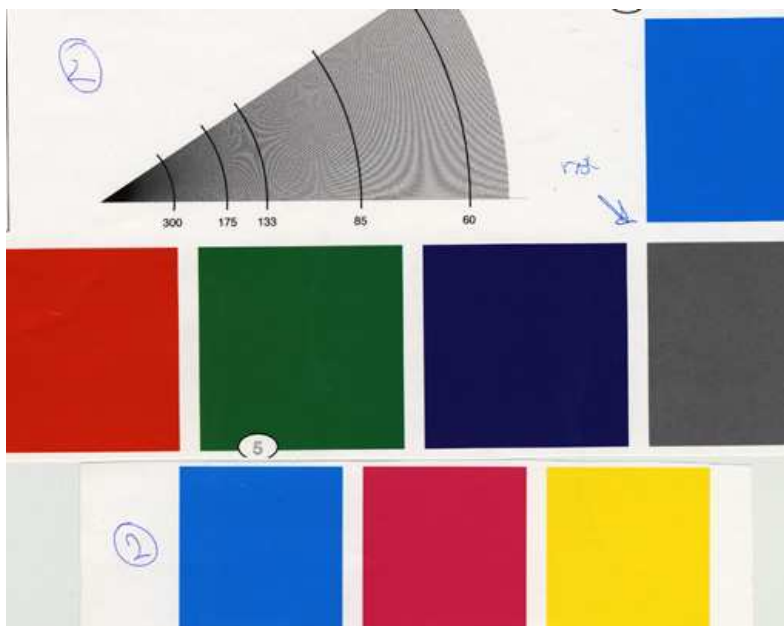
Figure 3.4. Verification of the calibration using 8 full tone colour patches printed on 3 different type of papers with varying glossiness.

3.3 Grey balancing

Due to uneven spectral sensitivities in the scanner's sensors, it will record unbalanced grey levels. This can be compensated for by using *grey balanced RGB* values. Grey balanced RGB values may or may not be included in the calibration process, see Section 5.1 for further discussions. The Grey balanced RGB is defined [14] by setting:

$$R = G = B = Y(or = L^*). \tag{3.1}$$

The Y- or L^*-values are grey scale reference values ranging from the absolute white point down to maximum density of the calibration chart, i.e. black colour. For example, such grey scale values are laid out on lover part of IT8.7/2-1993, Figure 3.1. Least-squares methods are used to fit the curves shown in Figure 3.5. The relation between (R, G, B)- and Y-values is expressed in Equation 3.2 and shown in the upper plot of Figure 3.5, and the Equation 3.3 which expresses the relation between (R, G, B)- and L^*-values, is shown in the lower plot of Figure 3.5. Then, to obtain Grey balanced RGB values, either Equation 3.2 or Equation 3.3, of the fitted curves are applied on all (R, G, B) values recorded by the scanner.

$$y = c_1 + c_2 \, x \tag{3.2}$$

$$y = c_3 + c_4 \sqrt[3]{x} \tag{3.3}$$
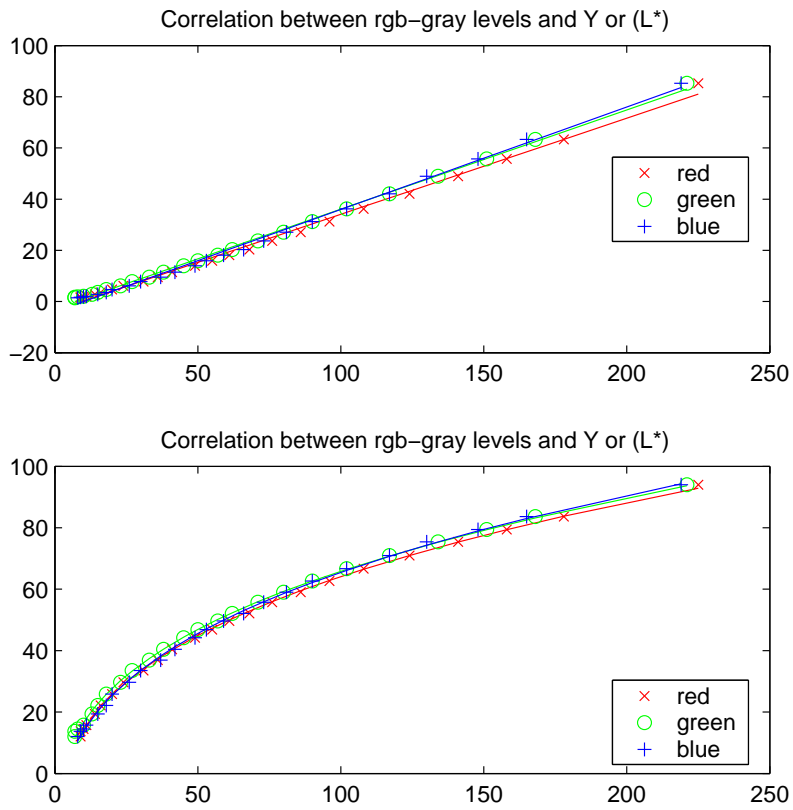
Figure 3.5. Upper plot shows relation between (R, G, B)- and Y-values, and the lower plot shows the relation between (R, G, B)- and L^*-values.

3.4 Calibration methods

Previous work done on colour scanner calibration techniques, described in [27], [22],[14], [15], [16] and [9], is the basis of determining the calibration function, $\mathcal{F}_{scan}$, in Equation 2.12. The calibration process is illustrated in Figure 3.6 and is further described in Section 2.3.2. The reader may notice that the calibration procedure goes in one way up to the point where the accuracy of the calibration is determined by comparison of calculated and measured CIE values, e.g. using Equation 2.9. The calibration function $\mathcal{F}_{scan}$ may either map (R, G, B) values to CIE (X, Y, Z) values, or directly map (R, G, B) values to CIE (L^*, a^*, b^*) values. The former values of mapping is then converted to (L^*, a^*, b^*) values via Equations 2.5, 2.6 and 2.7. Verification of the calibration is done in two steps. First, (L^*, a^*, b^*) values from scanned and measured calibration chart are compared, Step 4 and 5 in Figure 3.6. Secondly, other samples with, e.g. varying gloss properties which significantly differs from the calibration charts are scanned, evaluated with $\mathcal{F}_{scan}$ and then compared with the measured values.

Figure 3.6. Workflow of calibration process.

3.4.1 Linear polynomial calibration

A linear polynomial calibration assumes the existence of a linear relationship between the scanner's (R, G, B) colour space and the colorimetric (X, Y, Z) colour space, which in this case is the only possible target colour space. An alternative would be using (L^*, a^*, b^*) space as target, which in this case is not possible because of its inherit non-linearity. The linear relationship is expressed as:
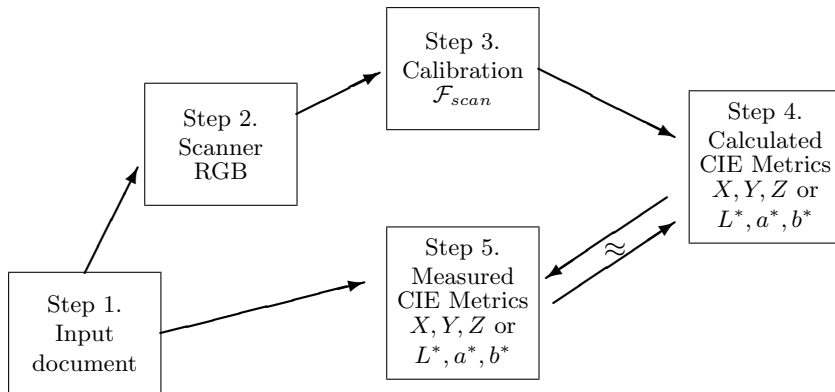
$$
\begin{pmatrix} R_1 & G_1 & B_1 \\ \vdots & \vdots & \vdots \\ R_M & G_M & B_M \end{pmatrix} \begin{pmatrix} a_{11} & a_{12} & a_{13} \\ a_{21} & a_{22} & a_{23} \\ a_{31} & a_{32} & a_{33} \end{pmatrix} \approx \begin{pmatrix} X_1 & Y_1 & Z_1 \\ \vdots & \vdots & \vdots \\ X_M & Y_M & Z_M \end{pmatrix}
\tag{3.4}
$$

where M is the number of samples in the calibration chart. A Least-squares method, see Appendix A, is then applied to find the coefficients $a_{11} \ldots a_{33}$ of the matrix, and the final (L^*, a^*, b^*) values are calculated with Equations 2.5, 2.6 and 2.7.

3.4.2 Calibration with artificial neural network

An artificial neural network, ANN, can be seen as a black box that "learns" a function by evaluating the relationship between a set of input data (R, G, B), called patterns, and output data (L^*, a^*, b^*), called targets. The black box mostly contains weights, actually real numbers, that are adjusted during the iterative process of training. After the training the ANN is ready to evaluate unseen input data, i.e. act like a mathematical function. This type of training, where the correct pattern and target relationship is evaluated a priori, is called supervised learning. There are also other types of ANN:s which learns only from the input data, called unsupervised learning. This thesis only deals with the former type. A well trained ANN should be able to generalize unseen data correctly, see Figure 3.9. In other words, the ANN should be able to evaluate noisy input data the same way as if the data would have been seen without noise.

The idea of an artificial neural network is to imitate the behaviour of the *neurons* in the human brain. The brain contains millions of neurons interconnected to each other where one neuron is affected through input from other neurons. This model is adapted into ANN, where the neuron is represented by the more simplified node, see Figure 3.7. The node in Figure 3.7 contains inputs $x_1, x_2, \cdots, x_M$ and the bias $b = 1$. The input is represented as a column vector $\mathbf{x}$ and output target is represented by vector $\mathbf{y}$. Every input component x_i is multiplied with a weight w_i, whose values are real numbers. Then, the activation of the node is calculated as the weighted sum of its inputs:

$$
a(\mathbf{x}) = \sum_{i=1}^{M} w_i x_i + \theta, \text{ where } \theta = w_{M+1} b.
\tag{3.5}
$$

The last term θ is the product of the bias, which is tied to $b = 1$, and the bias weight w_{M+1}. The correct value of w_{M+1} is obtained during training. The value of

θ determines the offset in the activation function, $\phi(a)$, where the activation, $a(\mathbf{x})$, is fed into to the activation function whose output e.g. ranges from $-1 \leq y \leq +1$, see Figure 3.7. The shape of the activation function determines how strongly the Node should respond. The activation function can also be piecewise linear, or a -1 to +1 threshold function.

Several vertically aligned nodes form a layer, which further can be connected to subsequent layers, see Figure 3.8. Indices i, j, k are used when referring to current layer j, previous layer i and next layer k. In the scanner calibration, a two layer feed forward net with back-propagation was used. In literature, the first input layer is not counted and the net used is of feed forward type where the signal propagates from left to right, i.e. there are no feedback loops from output to inputs nodes. The learning algorithm is referred to as back-propagation.
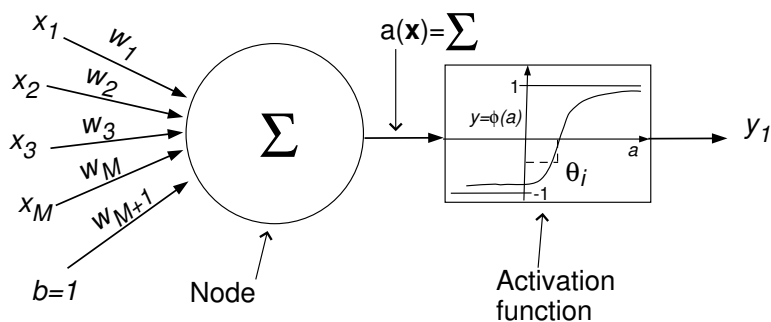
Figure 3.7. A node and the activation function in a artificial neural network.

Training the network

Here follows an overview of the theory involved in the training process. The interested reader may study the details about the back-propagation algorithm in [10], Bayesian learning in a feed forward ANN in [5], and the use of Levenberg-Marquardt algorithm when updating the weights in [8].

Training a network consists of presenting a set of patterns and targets in the form $\{\mathbf{p}_1, \mathbf{t}_1\}, \{\mathbf{p}_2, \mathbf{t}_2\}, \cdots, \{\mathbf{p}_Q, \mathbf{t}_Q\}$. Then the back-propagation is applied, which consists of two distinct passes of computation: the first referred to as the *forward pass*, and the second referred to as the *backward pass*. During the forward pass the input $\mathbf{p}_q$ is evaluated in the same way as a net that have completed training, i.e. with the weights remaining unaltered. Then, the backward pass changes the weights according to the calculated error. The backward pass changes the weights starting from the right nodes and propagating the changes to the left nodes.

The basic school book back-propagation algorithm is shown in Table 3.1, followed by the modified algorithm presented by Foresee and Hagan [5], shown in Table

3.2. Before we continue we should define a measure of how well the net is trained, i.e calculating the cost function, see Equation 3.6, which should be minimized.

The main purpose of the modified algorithm is to achieve good generalization capabilities, i.e. to avoid over fitting, see Figure 3.9. In other words, we want to find the correct mapping function during learning even though the input data is noisy. One building block in this process is regularization theory, proposed by Tikhonov in 1963 and another one is the use of Bayes' rule. The idea of regularization theory is that we can make the assumption that the input-output mapping function is smooth. Regularization theory will add an additional term to the cost function, see Equation 3.7, the sum of squared weights E_W which stabilizes the solution.

The modified algorithm uses Equation 3.8 as cost function, which also should be minimized. This is shown, using Bayes' rule, in [5]. Further, Bayes' rule is also used to calculate the most optimum values of α and β. The algorithm uses regularization with Bayes' rule to minimize the cost function $F = \beta E_D + \alpha E_W$, and the Levenberg-Marquardt algorithm to update the weights:

$$E_D = \frac{1}{2} \sum_{q=1}^{Q} (t_q - y_q)^2, \tag{3.6}$$

$$E_W = \|\mathbf{w}\|_2^2, \tag{3.7}$$

$$F(\mathbf{w}) = \beta E_D + \alpha E_W, \tag{3.8}$$

where $\mathbf{w} = [w_{11}^1, w_{12}^1, \cdots, w_{JI}^1, b_1^1, \cdots, b_J^1, \cdots, w_{11}^L, \cdots b_J^L]^T$,
and w_{ji}^m is the jith weight in the lth layer
of totally n weights and L layers.
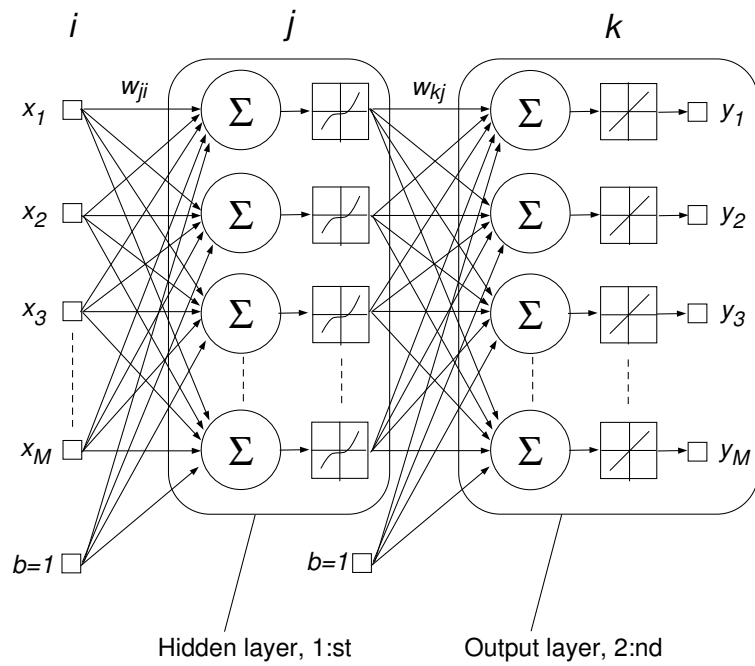
Figure 3.8. A principal sketch of a two layer feed forward artificial neural network. Indices i, j, k are used when referring to current layer j, previous layer i and next layer k. Notice the reversed order of indices which is the standard used in literature.
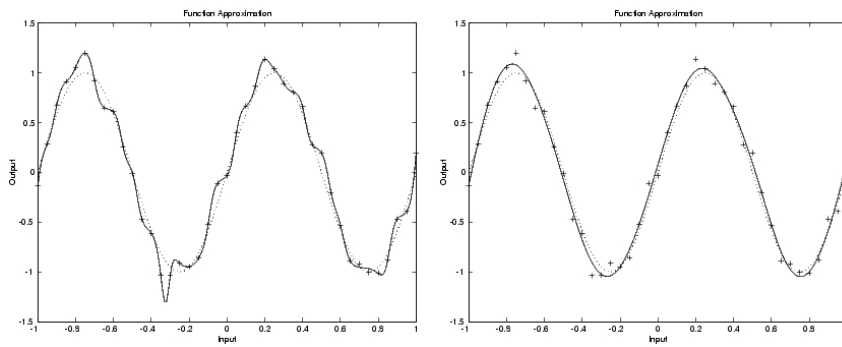
Figure 3.9. Left, a over fitted network. Right, a well generalized network.

Table 3.1. School book back-propagation algorithm.

1. Initialise weights randomly or use some other known method, e.g. Nguyen-Windrow method [21].

2. Present the input data in the nth iteration.

3. Perform the forward pass, i.e. calculate the output $y_j^{(l)}$ for the jth node in the lth layer, where $j = 1, 2, \ldots, N$ and $l = 1, 2, \ldots, L$. N is the number of nodes in the lth layer and L is the number of layers.

   - $y_j^{(l)} = \phi^{(l)}(a_j^{(l)})$
   - $a_j^{(l)} = \sum_{i=1}^{M} w_{ji}^{(l)} y_i^{(l-1)} + w_{j(i+1)}^{(l)} b^{(l)}$
   - Input $x_i = y_i^{(0)}$, and Output $y_j = y_j^{(L)}$

4. Start the backward pass with the computation of the output error signal: $e_j^{(L)} = t_j - y_j^{(L)}$ for all js in the rightmost layer L.

5. Compute the local error gradient δ_j where

$$
\delta_j^{(l)} = \begin{cases} e_j^{(L)} \phi_j'(a_j^{(L)}) & \text{when } l = L \text{ otherwise:} \\ \phi_j'(a_j^{(l)}) \sum_{k=1}^{O} \delta_k^{(l+1)} w_{kj}^{(l+1)}. \end{cases} \tag{3.9}
$$

   O is the number of nodes in the kth layer and ϕ' is the differentiate of the activation function. This requires that the activate function must be differentiable.

6. Adjust the weights according to the generalized delta rule [24]:

$$
\Delta w_{(n+1)ji}^{(l)} = \alpha \Delta w_{(n)ji}^{(l)} + \eta \delta_j^{(l)}
$$

$$
w_{(n+1)ji}^{(l)} = w_{(n)ji}^{(l)} + \Delta w_{(n+1)ji}^{(l)} \tag{3.10}
$$

   where $\alpha \approx 0.9$ is momentum term, and $\eta \approx 0.01$ is the learning rate.

7. Iterate steps 2 through 6 until convergence is obtained.

Table 3.2. Modified back-propagation algorithm.

1. Initialise $\alpha = 0$, $\beta = 1$ and weights using the Nguyen-Windrow method [21].

2. Evaluate the input during the forward pass and achieve output signal y_q.

3. Take one step in the Levenberg-Marquardt algorithm [8] to minimize $F(\mathbf{w}) = \beta E_D + \alpha E_W$ with respect to $\mathbf{w}$.

4. Compute the effective number of parameters $\gamma = N - 2\alpha \operatorname{tr}(\mathbf{H})^{-1}$, where $\mathbf{H}$ is Hessian matrix approximated in [8] as $\mathbf{H} = \nabla^2 F(\mathbf{w}) \approx 2\beta \mathbf{J}^T \mathbf{J} + 2\alpha \mathbf{I}$. N is the number of free parameters, i.e. the size of $\mathbf{w}$. Matrix J is the Jacobian matrix, see Appendix B.

5. Compute new estimates for $\alpha = \frac{\gamma}{2E_D(\mathbf{w})}$ and $\beta = \frac{N-\gamma}{2E_D(\mathbf{w})}$

6. Iterate steps 2 through 5 until convergence.

The implementation of ANN

The setup of the ANN consists of two layers, 3 input nodes, 8 to 10 hidden nodes and 3 output nodes. The implementation of the modified algorithm used is MATLAB's Neural Network Toolbox (version 4.0.2, R13). This implementation differs in one aspect from the examples described in [5]. In the implementation, the parameters E_D and E_A do not stay constant with the increasing number of hidden nodes, as they do in [5]. However, this seems not to be a problem, because the results presented in 4.1.2 are the same when the number of hidden nodes are increased. All inputs are scaled to [-1,1] interval. The scaling functions, `premnnmx` and `postmnmx`, included with the toolbox has been replaced with functions, `normalize` and `renormalize`. These use the min and max value calculated over all input nodes, instead of, as in the toolbox, using three separate min and max values for each of the input nodes. Since each input in ANN corresponds to one of the (R, G, B) channels from the scanner, where each channel may record a value between 0 and 255, it would be incorrect to treat each channel as an independent input. This is the case when using the normalization functions included with the toolbox. The activation function, see Figure 3.10, in the hidden node is the `tansig` function:

$$\phi(a) = \frac{2}{1 + e^{-2a}} - 1, \tag{3.11}$$

and for the output nodes, the `purelin` function:

$$\phi(a) = a. \tag{3.12}$$
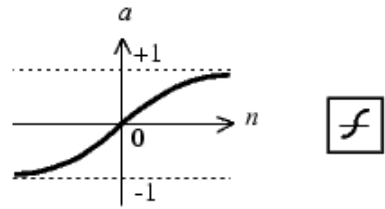
$$a = tansig(n)$$

Tan-Sigmoid Transfer Function
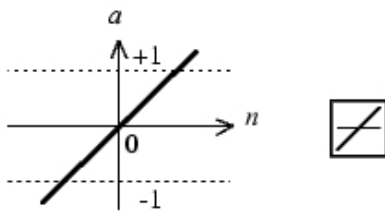
$$a = purelin(n)$$

Linear Transfer Function

Figure 3.10. Top, activation function used in hidden nodes. Bottom, activation function used in output nodes.

3.4.3 Non-linear polynomial regression

This calibration is based on the methodology described by Kang [14], [15] and Hardeberg [9]. The approach is similar to the linear calibration, Section 3.4.1, with the exception that the polynomials are non-linear. *Multiple regression* is applied on the non-linear polynomial to find $\mathcal{F}_{scan}$, Equation 2.12. We start with a multiple regression of a six term polynomial,

$$P(R,G,B) = a_1 R + a_2 G + a_3 B + a_4 RG + a_5 GB + a_6 RB, \tag{3.13}$$

which is written as an overdetermined system of equations of M inputs in matrix form:

$$\begin{pmatrix} R_1 & G_1 & B_1 & RG_1 & GB_1 & RB_1 \\ \vdots & \vdots & \vdots & \vdots & \vdots & \vdots \\ R_M & G_M & B_M & RG_M & GB_M & RB_M \end{pmatrix} \begin{pmatrix} a_{11} & a_{12} & a_{13} \\ a_{21} & a_{22} & a_{23} \\ a_{31} & a_{32} & a_{33} \\ a_{41} & a_{42} & a_{43} \\ a_{51} & a_{52} & a_{53} \\ a_{61} & a_{62} & a_{63} \end{pmatrix} \approx$$

$$\approx \begin{pmatrix} X_1 & Y_1 & Z_1 \\ \vdots & \vdots & \vdots \\ X_M & Y_M & Z_M \end{pmatrix}. \tag{3.14}$$

This is solved with QR-factorisation, see Appendix A. Then, the polynomials are extended with additional terms, more exactly 11, 14 and 20 terms, which is shown in Equations 3.15, 3.16 and 3.17. The reason for this is that we want to improve the accuracy of conversion from (R, G, B) to the independent CIE colour spaces, (X, Y, Z) or (L^*, a^*, b^*). Finally, we also pre-process the (R, G, B) values by extracting the third root, $\sqrt[3]{RGB}$.

$$P(R,G,B) = a_0 + a_1 R + a_2 G + a_3 B + a_4 RG + a_5 GB + $$
$$+ a_6 RB + a_7 R^2 + a_8 G^2 + a_9 B^2 + a_{10} RGB \tag{3.15}$$

$$P(R,G,B) = a_0 + a_1 R + a_2 G + a_3 B + a_4 RG + a_5 GB + a_6 RB + $$
$$+ a_7 R^2 + a_8 G^2 + a_9 B^2 + a_{10} RGB + a_{11} R^3 + a_{12} G^3 + a_{13} B^3 \tag{3.16}$$

$$P(R,G,B) = a_0 + a_1 R + a_2 G + a_3 B + a_4 RG + a_5 GB + a_6 RB + $$
$$+ a_7 R^2 + a_8 G^2 + a_9 B^2 + a_{10} RGB + a_{11} R^3 + a_{12} G^3 + a_{13} B^3 + $$
$$+ a_{14} RG^2 + a_{15} R^2 G + a_{16} GB^2 + a_{17} G^2 B + a_{18} RB^2 + a_{19} R^2 B \tag{3.17}$$

Chapter 4

Results

4.1 Results of different calibration methods

The first type of measurement on how well a calibration method performs is done on the reference calibration sheet, see Section 3.2.1. In other words, a verification of the calibration function is done on the same data that was used to establish the calibration. The second type of evaluation is carried out on the verification material described in Section 3.2.2. This type of material is used as an indicator of the accuracy of the calibration process that resembles a real world situation where other factors, described in second paragraph of Section 3.1, affect the result.

Calibrations are both done towards the (X, Y, Z) and (L^*, a^*, b^*) colour space. When calibration is done using (L^*, a^*, b^*) colour space and polynomial calibration, the input data, (R, G, B) scanner values, is pre-processed by extracting the third root, i.e. $\sqrt[3]{RGB}$. In cases when calibration is carried out with artificial neural networks, the input data is instead normalized to values in the [-1,1] interval.

4.1.1 Linear polynomial calibration

In the first case, the calibration is carried out via (X, Y, Z) colour space and then mathematically transformed, using Equations 2.5, 2.6 and 2.7. In the second case, we use (L^*, a^*, b^*) as the target colour space. The results of two different colour space targets are shown in Figure 4.1. In Figure 4.1 ΔE is shown, calculated
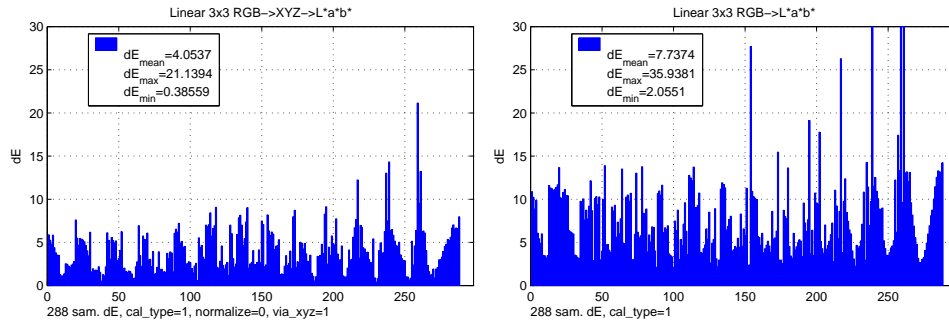
Figure 4.1. Result of linear polynomial calibration using (X, Y, Z) and (L^*, a^*, b^*) colour space.

according to Equation 2.9. In the same legend, the maximum, minimum and average ΔE values are also shown. No more test were conducted using the linear polynomial calibration due to the poor results presented in Figure 4.1. Also, when input data is grey balanced no improvement in accuracy is achieved.

4.1.2 Calibration with artificial neural network

We start by evaluating how the ANN performs on the reference calibration material, see Section 3.2.1. Also, the results with increasing number of hidden nodes are shown in Figures 4.2 and 4.3. The aim of testing the ANN with different amounts of hidden nodes is to find the correct threshold, see discussions in Section 3.4.2, where the number of hidden nodes used above the threshold will not make any significant improvement of the calibration result. Moreover, we observe, in the plots on the left sides of Figures 4.2 and 4.3, that calibrating using the intermediate (X, Y, Z) colour space, give rise to a lot of spikes in the subsequently calculated (L^*, a^*, b^*) values.
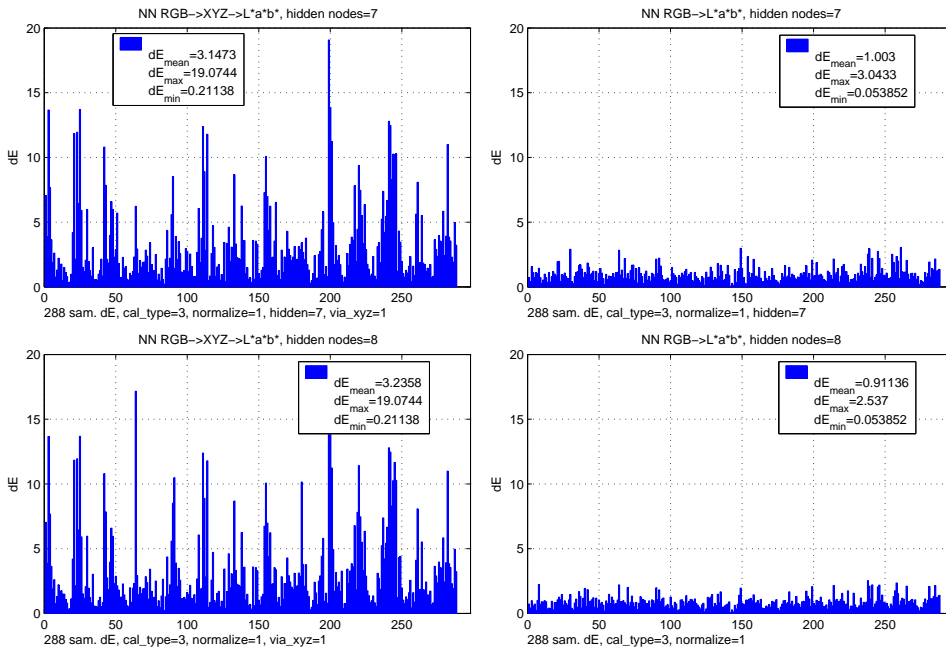
Figure 4.2. Result of ANN calibration with 7 and 8 hidden nodes. Left side shows result of calibration via the (X, Y, Z) colour space and the right side shows the calibration made directly towards the (L^*, a^*, b^*) colour space.

The calibration with ANN is also evaluated using the verification material, Section 3.2.2, which consist of 40 coloured halftone samples and the results are presented in Figure 4.4. The calibration is carried out directly towards (L^*, a^*, b^*) colour space. The mean colour difference, ΔE_{mean}, using either 288 or 338 reference samples, is 3.19 and 2.96 respectively, i.e. a difference of 0.23 units. The maximum colour difference error, ΔE_{max}, in the case of 288 and 338 reference samples used, is 10.47 and 8.94 respectively, which results in a difference of 1.53 units. The maximum error belongs to one of three peaks, numbered 17, 30 and 34, in Figure 4.4. The three outliers are saturated greenish colours which are marked with circles in Figure 3.3 on page 18.
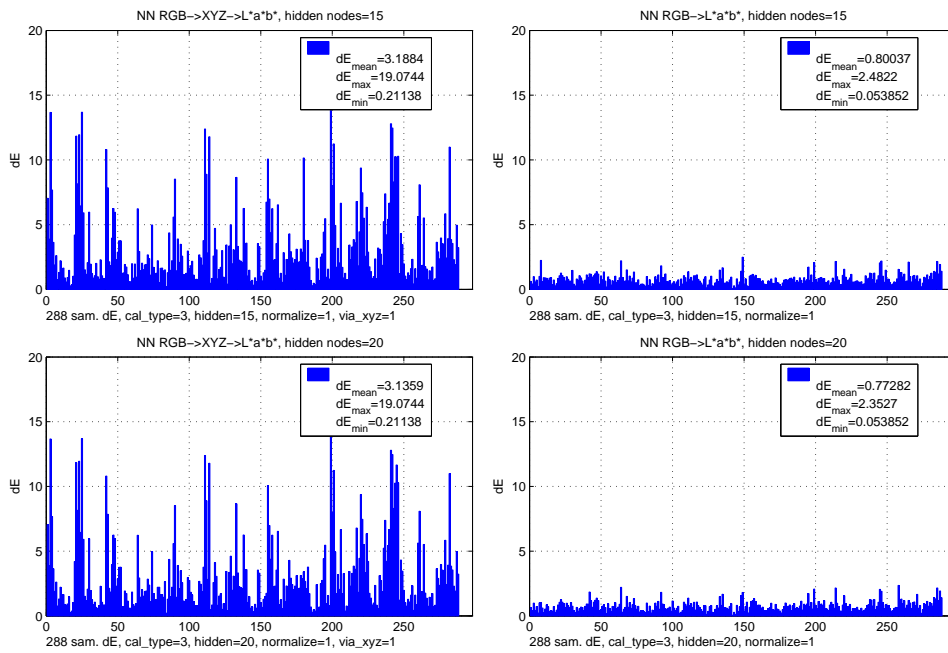
Figure 4.3. Result of ANN calibration with 15 and 20 hidden nodes. Left side shows the result of calibration via the (X, Y, Z) colour space and the right side shows the calibration when carried out directly towards the (L^*, a^*, b^*) colour space.

Figure 4.4. Verification of ANN calibration – Scanned halftone prints. Left and Right side shows the result of using 288 and 338 reference samples respectively.

The second type of verification material, described in Section 3.2.2, was also used to verify the accuracy of the ANN method. The material consists of 8 full tone colour patches printed on 3 different types of papers. The colours in this material are located close to the boundaries of the (L^*, a^*, b^*) colour space, where maximum colour gamut is defined by the reference calibration material.
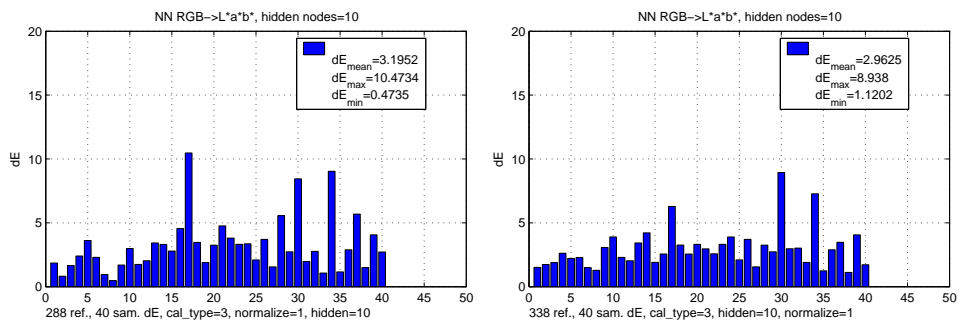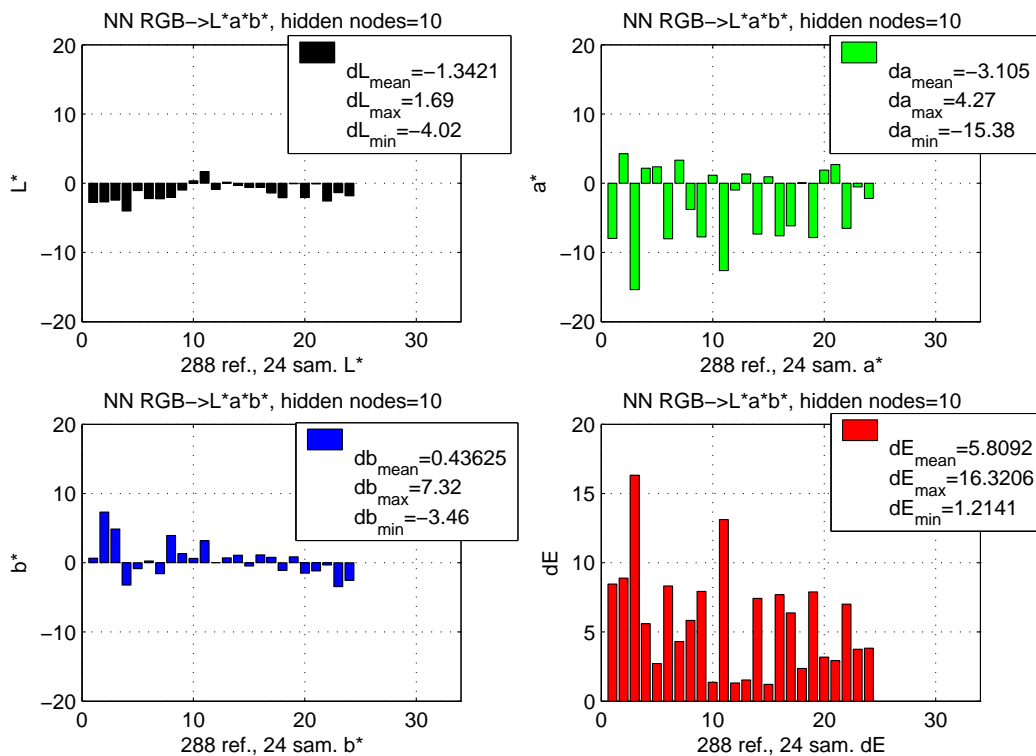

Figure 4.5. Verification of ANN calibration – Scanned full tone prints.

The first run using the IT8 as the calibration reference, see Section 3.2.1, resulted in a ΔE_{mean} and ΔE_{max} of 5.81 and 16.32 units, see Figure 4.5. To improve the calibration, the additional 50 NCS surfaces was added to the calibration reference material. The results from the calibration with the extended material are presented in Figure 4.6. There is an improvement of the ΔE_{mean} from 5.81 to 5.69 and ΔE_{max} from 16.32 to 15.91 shown on the left side of Figure 4.6. Moreover, when performing the grey balancing, see right hand side of Figure 4.6, the ΔE_{mean} was slightly worse, a value of 5.96, when compared using the 288 reference samples. Although, grey balanced RGB values gave the so far lowest value of ΔE_{max}, 15.57. The outlier that mostly contributes to the overall error is the third sample, which also, in this case is greenish as in the previous test with halftone prints shown in Figure 3.3.
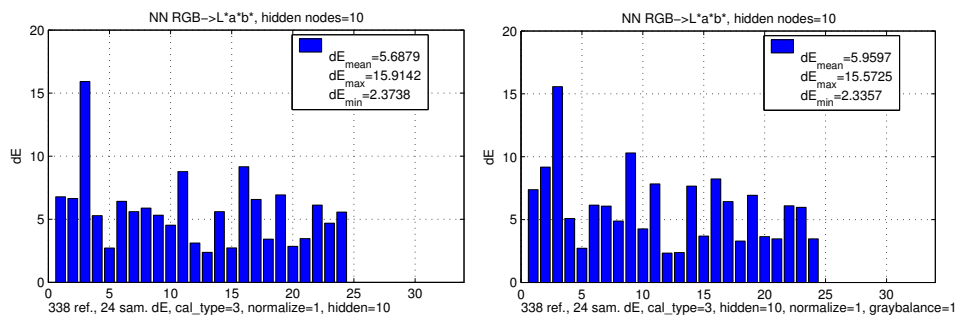
Figure 4.6. Verification of ANN calibration – Scanned full tone prints. In this case left side contains 338 reference samples and the right side also includes grey balancing.

4.1.3 Non-linear polynomial regression

As in the previous Section, we start to evaluate the calibration methods using the reference material described in Section 3.2.1. We begin with a 6 term polynomial to find the calibration function, and then extend the polynomial to 11, 14 and 20 terms, as described in Section 3.4.3. The result of using 6 and 11 terms is presented in Figure 4.7. From the upper left plot in Figure 4.7 we can read out that the ΔE_{mean} and ΔE_{max} is 2.68 and 17.83 respectively. These results are based on the case when the calibration is carried out via the intermediate (X, Y, Z) colour space. To the right in same figure, using the (L^*, a^*, b^*) colour space as target calibration, we observe that ΔE_{mean} and ΔE_{max} is 3.96 and 20.92 respectively. In the lower
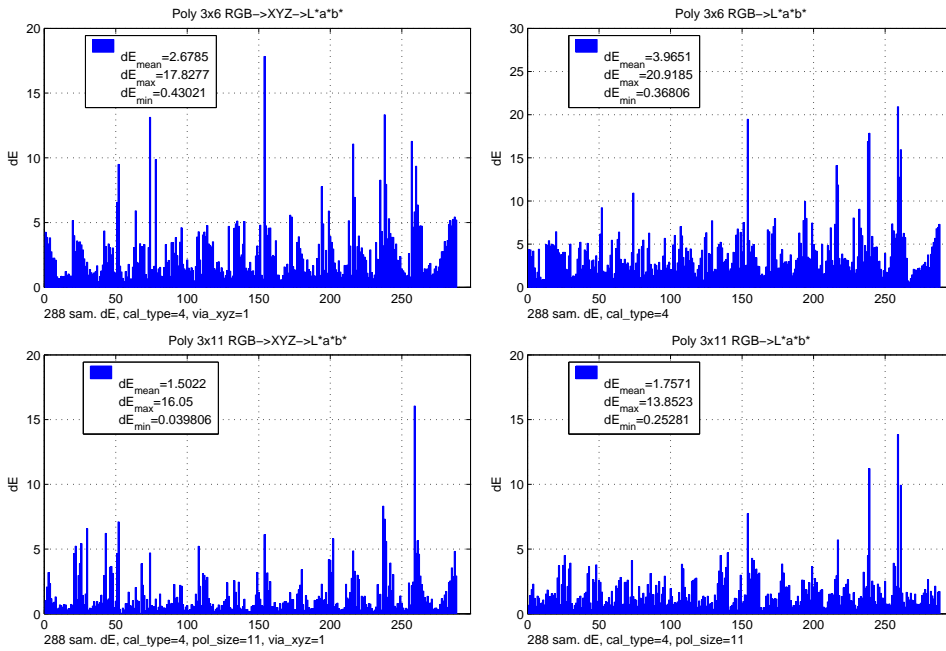
Figure 4.7. Result of non-linear polynomial calibration with 6 and 11 terms.

left and lower right plots, of Figure 4.7, are the results of calibration with 11 term polynomial presented. The results of ΔE_{mean} and ΔE_{max} are 1.50 and 16.05, using the intermediate (X, Y, Z) colour space, and using target (L^*, a^*, b^*) colour space, we obtain a ΔE_{mean} equal to 1.75 and a ΔE_{max} equal to 13.85. The difference between using the intermediate (X, Y, Z) colour space and the target (L^*, a^*, b^*) colour space is 0.25 units lower in ΔE_{mean} with the former type of calibration and 2.2 units lower in ΔE_{max} with the latter type of calibration.

Verification of the calibration with 14 and 20 terms is presented in Figure 4.8. We see that results of ΔE_{mean} and ΔE_{max}, using the intermediate (X, Y, Z) colour space with 14 term polynomial, are 0.96 and 4.52. The corresponding result of using the target (L^*, a^*, b^*) colour space are 1.43 and 7.00, seen in the upper right plot of Figure 4.8. The results from the last type of calibration with a 20 term polynomial

are presented in lower part of Figure 4.8. The left plot shows the results of using the intermediate (X, Y, Z) colour space, which are 0.85 and 4.49 for ΔE_{mean} and ΔE_{max}. In the right plot are the results, when using the target (L^*, a^*, b^*) colour space, shown for ΔE_{mean} and ΔE_{max} which are 0.72 and 2.62. Using the target (L^*, a^*, b^*) colour space, we obtain lower values for both ΔE_{mean} and ΔE_{max}, which are 0.13 and 1.88 units lower than using the intermediate (X, Y, Z) colour space.
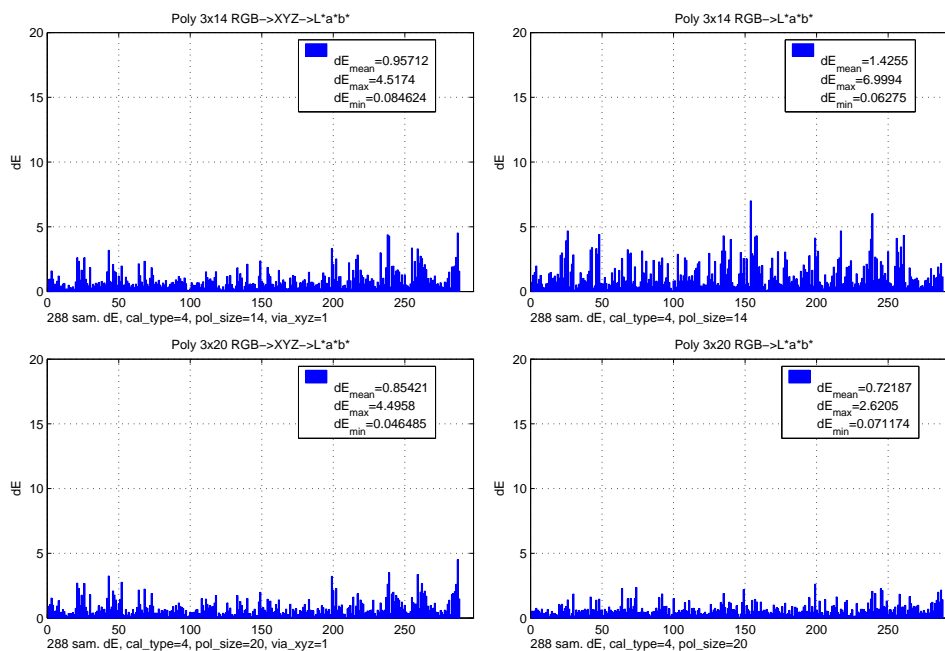
Figure 4.8. Result of non-linear polynomial calibration with 14 and 20 terms.

The next results, presented in Figure 4.9 show how the polynomial calibration with 20 terms performs using the verification data seen in Figure 3.3. On the left side of the Figure 4.9, we observe that the ΔE_{mean} is 3.11 and ΔE_{max} is 8.93 using 288 samples in the reference material, see Section 3.2.1. The same verification material was used to evaluate the same type of calibration on a reference material extended with 50 NCS surfaces, described in Section 3.2.1, giving a total of 338 samples used in the reference material of the calibration. The results are presented on the right side of Figure 4.9, yielding a ΔE_{mean} of 2.96 and ΔE_{max} of 9.1. This is an improvement of +0.15 units and an impairment of -0.17 units compared with the 288 samples verification calibration used. The outliers, sample 17, 30 and 34, seen in Figure 4.9 are the same as the ones observed in Figure 4.4, and described in Section 4.1.2.
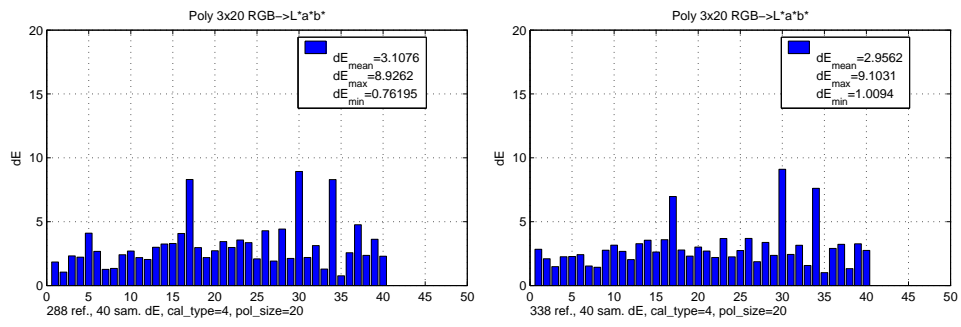
Figure 4.9. Verification of polynomial calibration – Scanned halftone prints. Left and Right side shows the result of using 288 and 338 reference samples respectively.

The last type of verification is made on the 24 full tone colour patches, described in Section 3.2.2 and seen in Figure 3.4. The results from this test are presented in Figure 4.10. The ΔE_{mean} and ΔE_{max} is 6.39 and 15.58 respectively. Also, the same outlier, sample number 3, is observed as in Figure 4.5. In the same figure, looking at upper right plot, which shows the a^* coordinate axis, we see that most of the fluctuations of the errors originates from Δa^* contribution. The IT8 is used as
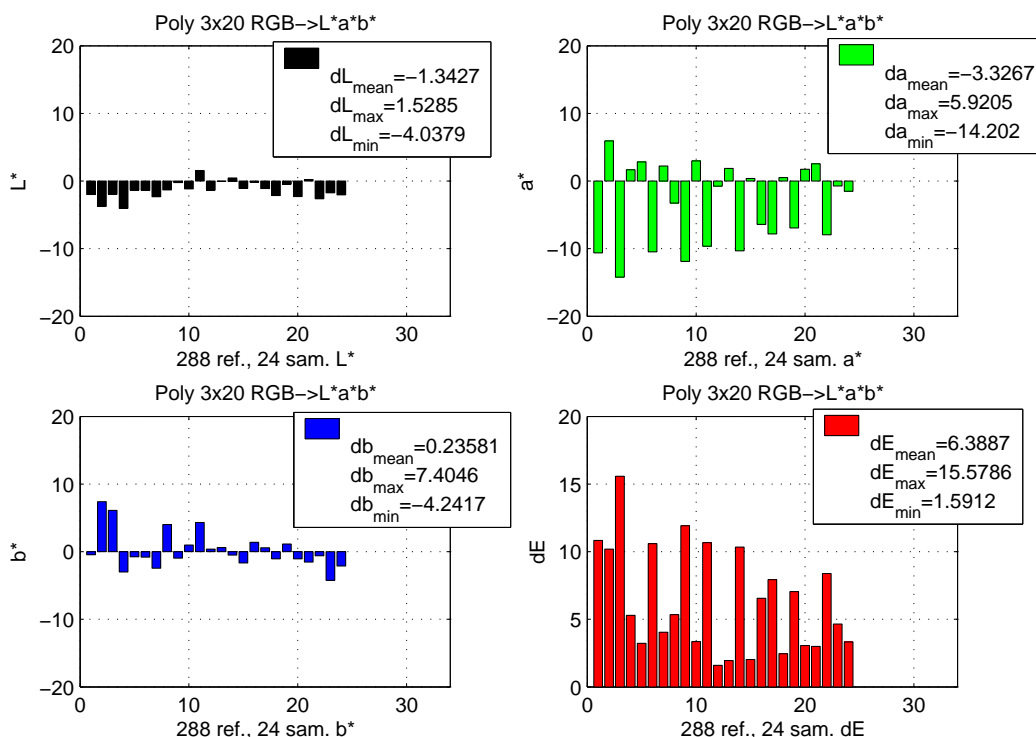
Figure 4.10. Verification of polynomial calibration – Scanned full tone prints.

reference material in the calibration, and to improve the calibration for these specific samples, we add the 50 NCS surfaces, described in Section 3.2.1 to the reference material. Moreover, to see if any improvement in the calibration process could be achieved, the scanned (R, G, B) values were also grey balanced. The results from these modifications are presented in Figure 4.11. In the figure, it can be observed that, in case of non grey balanced and grey balanced (R, G, B) values, the ΔE_{mean} and ΔE_{max} are the same, i.e. 5.90 and 15.21.

4.1.4 A summary of the results

Here follows a summary of the resutls from the ANN and the non-linear polynomial calibration. The results from both types of methods, calibration with reference and verfication material, are presented in Table 4.1. In Table 4.1, only the results from calibrating towards the (L^*, a^*, b^*) target colour space are presented, see Section
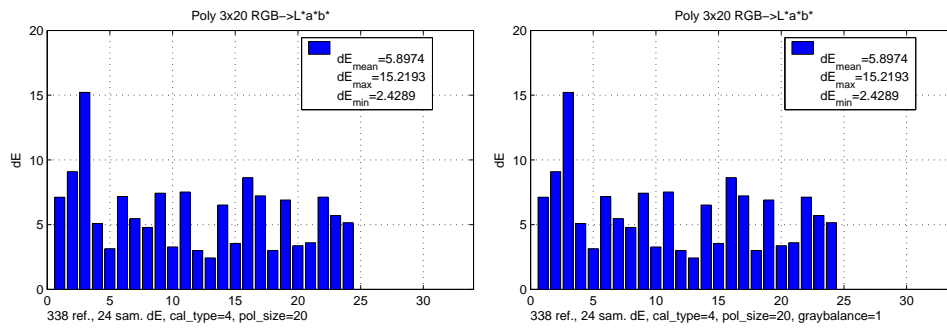
Figure 4.11. Verification of polynomial calibration – Scanned full tone prints. In this case left side contains 338 reference samples and the right side also includes grey balancing.

5.1 for more discussions. A dash in the verification material column of Table 4.1 denotes calibration with only the reference material.

Table 4.1. A summary of the results of polynomial and ANN calibration methods, using (L^*, a^*, b^*) as the target colour space.

Method	Ref. material	Ver. material	ΔE_{mean}	ΔE_{max}
ANN 7 h. nodes	288 samples	–	1.00	3.04
ANN 8 h. nodes	288 samples	–	0.91	2.54
ANN 15 h. nodes	288 samples	–	0.80	2.48
ANN 20 h. nodes	288 samples	–	0.77	2.35
ANN 10 h. nodes	288 samples	40 samples	3.19	10.47
ANN 10 h. nodes	338 samples	40 samples	2.96	8.94
ANN 10 h. nodes	288 samples	24 samples	5.81	16.32
ANN 10 h. nodes	338 samples	24 samples	5.69	15.91
ANN 10 h. nodes with grey balancing	338 samples	24 samples	5.96	15.57
Pol. 6 terms	288 samples	–	3.96	20.92
Pol. 11 terms	288 samples	–	1.75	13.85
Pol. 14 terms	288 samples	–	1.42	7.00
Pol. 20 terms	288 samples	–	0.72	2.62
Pol. 20 terms	288 samples	40 samples	3.11	8.93
Pol. 20 terms	338 samples	40 samples	2.96	9.10
Pol. 20 terms	288 samples	24 samples	6.39	15.58
Pol. 20 terms	338 samples	24 samples	5.90	15.21
Pol. 20 terms with grey balancing	338 samples	24 samples	5.90	15.21

Chapter 5

Discussions and conclusions

5.1 Discussions

5.1.1 Calibrate towards (X, Y, Z) or (L^*, a^*, b^*) colour space?

The first question that probably has arised so far is: should we use the (X, Y, Z) or the (L^*, a^*, b^*) colour space as target in the calibration process? The reason for asking this question is that when carrying out calibration tests using the intermediate (X, Y, Z) colour space, large errors have been observed in colours with low (X, Y, Z) values. To find the cause of these erros, we investigate the sensitivity of Equations 2.5, 2.6 and 2.7. Further, we assume that we have scanned the IT8, see Figure 3.1, and want to verify the calibration function using the reference material. If we assume a worst case scenario where there is e.g. interference in the recording process which give rise to an absolute error of $+0.5$ units in the Y component and -0.5 units in the Z component, and where the X component is intact. Then, we evaluate the disturbed and undisturbed input with Equations 2.5, 2.6 and 2.7 and calculate, using Equation 2.9, the Euclidean distance between the compared inputs. The result of these calculations are presented in Figure 5.1. The plots in Figure 5.1 indicate a varying magnitude of the error ranging over the whole colour *gamut* of the IT8. The grey scale patches in the lower part of the IT8 are achromatic, i.e. the X, Y and Z components have approximately the same values. Looking at error of the grey scale patches, right side of Figure 5.1, we observe that the error increases with smaller magnitudes of (X, Y, Z) values. The conclusion that we can make from this observation is that the same disturbance in the input will have a greater impact on the erros of colours with low luminance, i.e. have low (X, Y, Z) values. In other words, the mathematical transformation from (X, Y, Z) colour space to (L^*, a^*, b^*) colour space is ill conditioned, see discussions in [11].

The results from Figure 5.1 also explain most of the spikes seen on the left sides of Figures 4.2 and 4.3 when calibration are carried out with the artificial neural network. Since the goal of the ANN, see Section 3.4.2, is to find a generalized function, the points in the function chosen by the ANN will induce an error that is propagated and increased through the mathematical transformation from (X, Y, Z)
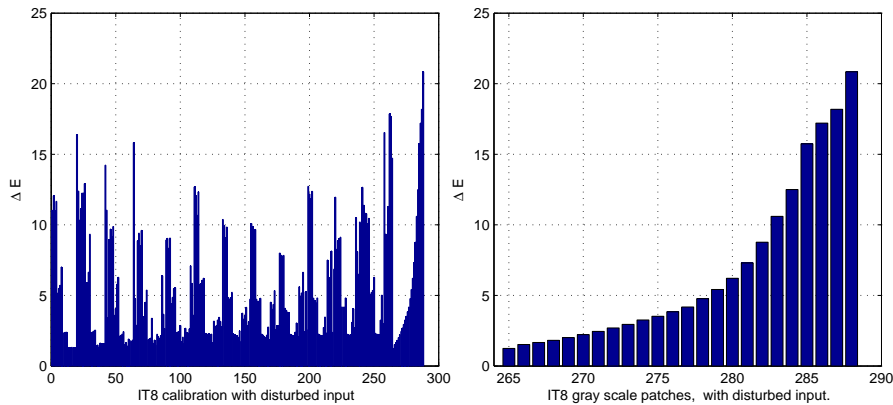
Figure 5.1. Left, the IT8 with disturbed input. Right, a close up of disturbed grey scale patches.

to (L^*, a^*, b^*).

The same type of errors are also seen on the left side of Figure 4.7 when using a polynomial calibration with 6 and 11 terms. When using a 14 and 20 term polynomial, see left side of Figure 4.8, the error decreases substantially, and it seems that using the intermediate (X, Y, Z) colour space with 14 term polynomial will yield a better result than directly calibrating towards the (L^*, a^*, b^*) colour space, which results are seen on upper right side of Figure 4.8. However, in the case of using a 20 term polynomial the results are better with the target (L^*, a^*, b^*) colour space, presented on the lower right side of Figure 4.8. The improved result using the 14 term polynomial is due to that the function in this case closer fits the actual points of the reference calibration material. Nevertheless, if the input data is slightly disturbed in same way as described in beginning of this section, the result of the calibration will not be satisfactory.

Finally, the *condition number* of the matrix calculated in Equation 3.17 when using multiple regression, is less than 3. In reality, compared with the sensitivity of calculated (L^*, a^*, b^*) values, this means that a small relative change in input results in a small relative change in output. In other words, the calculated matrix, using the (L^*, a^*, b^*) as target colour space, in the polynomial curve fit is much more robust than calculating (L^*, a^*, b^*) values using the intermediate (X, Y, Z) colour space.

5.1.2   Analysis of calibration with verification material

By analysing the results from the verification of the calibration, we obtain similar results, presented in Figures 4.4, 4.9, 4.5 and 4.10, when either using artificial neural networks or multiple regression of polynomials. The average results of the calibration presented in Figures 4.4 and 4.9, are good, i.e. they meet the goal of desired accuracy of the calibration which is a $\Delta E < 5$. The overall error seen in Figures 4.5 and 4.10 almost meets the goal, but where the errors of the individual samples fluctuate, we try to investigate the cause of those.

A closer look at the results from the calibration test with the 40 halftone colours, seen in Figure 4.4 and 4.9, indicate the same outliers, i.e. sample 17, 30 and 34. Since we have used two independent approaches, it is highly improbable that error originates from the actual calibration method. One reason to this error, could be that the coordinates of the samples lay outside the colour gamut of the IT8. However, extending the reference material with the 50 NCS surfaces, whose (L^*, a^*, b^*) points enclose all the points of 40 halftone colours, does not yield any substantial improvements, see results on the right side of Figures 4.4 and 4.9. Still, there are fewer reference sample points in the outer parts than the inner parts of the (L^*, a^*, b^*) colour space, see [1]. The largest contributing factors to the errors are the flaws that non-colorimetric scanners suffers from, see Sections 2.3.1 and 3.1.

Now, analysing the results from the calibration, using the second type of verification material, i.e. the 24 full tone colour in Figure 3.4, we observe, in Figures 4.5 and 4.10, the same fluctuations of the errors. Also extending the reference material with the 50 NCS surfaces and performing grey balancing only slightly improves the results, presented in Figures 4.6 and 4.11. Let us therefore compare two almost identical (L^*, a^*, b^*) coordinates with their corresponding scanned (R, G, B) values. The (L^*, a^*, b^*) coordinates have been measured with the GREGTAG instrument, see Section 3.2.2. If the scanner is consistent both the corresponding (R, G, B) values should approximately be the same. In this case we compare the largest outlier, the green sample number 3 with the green sample 11 whose (L^*, a^*, b^*) values are [52, -61, 27] and [53, -67, 25] respectively, where the corresponding (R, G, B) values are [30, 89, 44] and [18, 81, 34]. At the first glance, we see that the R and B coordinates are much higher in the third sample, and doing a backward transformation from (L^*, a^*, b^*) to (R, G, B) indicates that a consistent value approximately should have been [18, 84, 33]. When visually examining the deviating sample, small bright areas are seen, which are strengthen under a certain viewing angle. The spectral sensors in a scanner are placed in an angle that is different from the gloss angle. But in this case, the viewing angle of the bright areas seen is different from the gloss angle. A reasonable explanation to this error is that the bright, glossy, areas contribute to the average luminance, and thereby yielding higher (R, G, B) values. Such type of problems are related to the construction of the scanner and are difficult to compensate for in the calibration process.

5.2 Conclusions

We have evaluated a couple of calibrations methods starting with a simple linear curve fit and ending with a multiple regression of a 20 term polynomial, the latter showing satisfying accuracy. Artificial neural network has also presented good results and suggests that the polynomial approach is appropriately implemented. Moreover, the Bayesian ANN has, opposite to the results presented in [16], shown good generalization properties. When comparing the performance of ANN with the other methods, it demands more computational time in the training process. An ANN with 10 hidden nodes takes approximately 20 seconds to train on a standard PC of today, whereas evaluation of input data is as good as in the case of the polynomial method. However, both methods will be computer and memory demanding on large input data, in which case it is advisory to pre-evaluate input data with one of the presented methods and enter the results in a 3D look-up table. A 3D look-up table is e.g. of size $9 \times 9 \times 9$ and uses some known interpolation method [15], to find values in between the pre-evaluated points. Finally, when it comes to choosing between the ANN and the 20 term polynomial calibration, we recommend to use the latter because of its simple implementation.

The two best performing calibration methods, multiple regression with a 20 term polynomial and Bayesian artificial neural network has shown high accuracy, i.e. $\Delta E_{mean} < 1$, when evaluating the methods on the reference material, see Figures 4.3 and 4.8, and $\Delta E_{mean} < 4$ when using the verification material, see Figures 4.4 and 4.9. We should not use the intermediate (X, Y, Z) colour space, but instead directly use the (L^*, a^*, b^*) as the calibration target. Preprocessing the input with grey balancing did not improve the calibration results in neither case, which means that it can be left out. The results have shown that observed errors mostly depend on external factors e.g. inconsistent recording of RGB values in the scanner which is due to the type of dye set and coating used, and to the reflective and transmissive characteristics of the samples [15].

Further, most of the calibration methods, described in [27], [16],[14] and [9], use the reference material to verify the accuracy of the calibration. This is a correct approach when we initially want to mathematically verify the accuracy of the calibration method in use. However, we have also chosen to extend the test of the calibration method by using the verification material, see 3.2.1, whose points differ from the reference material in (L^*, a^*, b^*) colour space, and thereby testing the generalization capabilities of the method. We also obtain results that better correspond to the aimed use of the calibration, see Section 1.1.

Additional work on this thesis could be to use other type of reference material. The reason for this is that the design of the IT8 has been aimed to "provide a reasonable measure of color gamut that is within the capability of modern color photographic papers", stated in [1]. In other words, the IT8 has been designed for calibration when scanning photographs. Since, we are interested in applying the calibration when measuring colour print mottle on printed paper consisting of full tone colours, it would be a good idea to manufacture a calibration chart with similar

surface properties as the samples that are to be measured. Also, in this case, the saturation of colours are higher on printed paper than on photographic paper used by the IT8. Another objection to the IT8 is that most of the mandatory points, see Section 3.2.1, are located close to the L^* axis, i.e. the fewer points in the outer parts of the (L^*, a^*, b^*) colour space.

The results presented in this thesis show that the calibration in some cases is highly accurate, see Figure 4.9 and in other cases slightly less accurate, see Figure 4.10. Nevertheless, as we are interested in examining the variations around a point, i.e. colour print mottle, in (L^*, a^*, b^*) colour space, it is not necessary to measure the colours of the scanned material with dead on precision ($\Delta E_{mean} < 1$). Therefore, we are satisfied to be almost correct ($\Delta E_{mean} < 5$) in the calibration as long as the measured samples do not show high glossiness, which can heavily affect the scanner's ability to record the correct (R, G, B) values ($\Delta E_{mean} > 10$).

Glossary

B

backward pass   Refers to the training step in an Artificial Neural Network where the weights are altered to find the correct mapping between input and output data, p. 23.

C

coefficient of variation of reflectance   A measure of print mottle which often is expressed as the ratio between the standard deviation and the mean value of reflectance, p. 13.

colorimetric   A property of a device which detects colours as the CIE standard observer, p. 16.

colour constancy   The human visual system's ability to perceive the same colour sensations under different conditions of illumination, p. 3.

condition number   The condition number of a matrix is a measure of how close a matrix is to being singular, i.e. $\det(A) = 0$. A matrix with a large condition number is nearly singular, whereas a matrix with a condition number close to 1 is far from being singular, p. 44.

F

forward pass   Refers to an evaluation of input in an Artificial Neural Network where the weights are kept unaltered, p. 23.

full tone   Refers to paper printed with full coverage of at least one of the process colours, CMYK, p. 2.

G

gamut   Defines the volume of all possible colours in a given printing environment, p. 16.

grey balanced RGB   A pre-processing step in calibration, where the scanned RGB values are calibrated to match a grey level reference, which ranges from absolute white to black colour, p. 19.

H

halftone   Refers to paper where the colour is built up of a grid of raster cells, where each cell is partially filled with the current colour, p. 16.

J

just noticeable difference (JND)   The smallest distinguishable colour difference that humans can perceive, p. 10.

M

mesopic vision   The type of vision that is enabled during medium light conditions, where both cones and rods are activated, p. 4.

metameric   Refers to metamers that are perceived to have the same colour under certain illumination conditions, p. 9.

metamerism   The amount of change in light illumination that is needed to cease metameric occurrence. A way of grading a metameric environment, p. 9.

metamers   Refers to the illuminated objects that participates in a metameric environment, p. 9.

multiple regression   Regression is a method for fitting a curve (not necessarily a straight line) through a set of points using some goodness-of-fit criterion. The most common type of regression is linear regression. A multiple regression is regression of values of a given variable in terms of two or more other variables, p. 29.

N

neurons   Cells in the human body that act as information carrier and transmits signals between different parts of the body. Most neurons are located in the brain, p. 22.

P

photopic vision   The type of vision that is enabled during high light conditions, where mostly cones are activated, p. 4.

S

scotopic vision The type of vision that is enabled during low light conditions, where only rods are activated, p. 4.

References

[1] American National Standards Institute, ANSI. *IT8.7/2-1993*. NPES The Association for Suppliers and Printing and Publishing, 1993. Graphic technology - Color reflection target for input scanner calibration.

[2] C. M. Bishop. *"Neural Networks for Pattern Recognition"*. Oxford University Press, 1st edition, 1995.

[3] C.-M. Fahlcrantz. *"On the Evaluation of Systematic Print Mottle"*. Licentiate thesis, Royal Institute of Technology (KTH), 2003.

[4] M. D. Fairchild. *"Color Apperance models"*. Addison Wesley, 1st edition, 1998.

[5] F.D. Foresee and M.T. Hagan. "Gauss Newton approximation to Bayesian learning". In *Proceedings of the 1997 International Joint Conference on Neural Networks*, volume 3, pages 1930–1935. Institute of Electrical and Electronics Engineers, Inc. IEEE, Jun 1997.

[6] G.A. Gescheider. *"Psychophysics: The Fundementals"*. Erlbaum Associates Publishers Mahwah New Jersey, 3rd edition, 1997.

[7] R. C. Gonzalez and R. E. Woods. *"Digital Imaging Processing"*. Prentice Hall, 2nd edition, 2002.

[8] M.T. Hagan and M.B. Menhaj. "Training Feedforward Networks with the Marquardt Algorithm". *IEEE Transactions on Neural Networks*, 5:989–993, Nov 1994.

[9] J. Y. Hardeberg. "Desktop Scanning to sRGB". In *Color Imaging: Device-Independent Color*, volume 3963, pages 47–57. SPIE Proceedings, Mar 1999.

[10] S. Haykin. *"Neural Networks A Comprehensive Foundation"*. Prentice Hall, 2nd edition, 1999.

[11] M. T. Heat. *"Scientific Computing: An Introductory Survey"*. McGraw-Hill, 1st edition, 1997.

[12] R. W. G. Hunt. *"Measuring Colour"*. Ellis Horwood, 1987.

[13] P.-Å. Johansson. *"Optical Homogenity of Prints"*. Doctoral thesis, Royal Institute of Technology (KTH), 1999.

[14] H. R. Kang. "Color Scanner Calibration". *Journal of Imaging Science and Techology*, 36:162–170, Mar 1992.

[15] H. R. Kang. *"Color technology for electronic imaging devices"*. SPIE - The international Society for Optical Engineering, 1st edition, 1997.

[16] H. R. Kang and P. G. Anderson. "Nerual network applications to color scanner and printer calibrations". *Journal of Electronic Imaging*, 1:125–135, Apr 1992.

[17] D. C. Lay. *"Linear Algebra and Its Applications"*. Addison Wesley, 1st edition, 1994.

[18] D.L. MacAdam. *"Color Measurement"*. Springer-Verlag Heidelberg New York Tokyo, 2nd edition, 1985.

[19] M. Mahy, L. van Eycken, and A. Oosterlinck. "Evaluation of uniform color spaces developed after the adoption of CIELAB and CIELUV". *Color Resarch and Application*, 19:105–121, Apr 1994.

[20] H. Mizes. "Graininess of Color Halftones". In *IS&Ts NIP16: 2000 International Conference on Digital Printing Technologies*, 2000.

[21] D. Nguyen and B. Windrow. "Improving the Learning Speed of 2-layer Neural Networks by Choosing Initial Values of the Adaptive Weights". In *Proceedings of the 1997 International Joint Conference on Neural Networks*, volume 3, pages 21–26. Institute of Electrical and Electronics Engineers, Inc. IEEE, Jul 1990.

[22] V. Ostromoukhov, R.D. Hersch, C. Pèraire, P. Emmel, and I. Amidror. Two Approaches in Scanner-Printer Calibration: Colorimetric Space-Based vs. "Closed-Lopp". In *Device-Independent Color Imaging*, volume 2170, pages 133–142. IS&T/SPIE NIP16: 2000 International Conference on Digital Printing Technologies, Feb 1994.

[23] S. E. Palmer. *"Vision Sience"*. The MIT Press, 1st edition, 1999.

[24] Y.-H. Pao. *"Adaptive Pattern Recognition and Neural Networks"*. Addison-Wesley, 2nd edition, 1989.

[25] S. Rydefalk and M. Wedin. *"Literaute Review on the Colour Gamut in the printing process"*. PFT-rapport 32, STFI, Svenska Träforksnings Institutet, 1997.

[26] H.J. Trusell and J.R. Sullivan. "A vector approach to color imaging systems". *Image Processing Algorithms and Techiques*, 1244:264–271, Feb 1990.

54

[27] H.J. Trusell and M.J. Vrhel. "Color scanner calibration via a neural network". In *Acoustics, Speech, and Signal Processing, ICASSP '99. Proceedings., 1999 IEEE International Conference on*, volume 6, pages 3465–3468. Institute of Electrical and Electronics Engineers, Inc. IEEE, Mar 1999.

[28] M. J. Vrhel and H. J. Trusell. "A Color Device Calibration: A Mathematical Formulation". *IEEE Transactions on Image Processing*, 8:1796–1806, Dec 1999.

Appendix A

Least-squares method

A preferable notation in books [17] of least squares data-fitting problem is:

$$\mathbf{A}\,\mathbf{x} \approx \mathbf{b} \tag{A.1}$$

In our case, Equation 3.4, presented in A.2, must be rewritten to conform with A.1, which is done in A.3.

$$
\begin{pmatrix}
R_1 & G_1 & B_1 \\
\vdots & \vdots & \vdots \\
R_M & G_M & B_M
\end{pmatrix}
\begin{pmatrix}
a_{11} & a_{12} & a_{13} \\
a_{21} & a_{22} & a_{23} \\
a_{31} & a_{32} & a_{33}
\end{pmatrix}
\approx
\begin{pmatrix}
X_1 & Y_1 & Z_1 \\
\vdots & \vdots & \vdots \\
X_M & Y_M & Z_M
\end{pmatrix}
\tag{A.2}
$$

$$
\begin{pmatrix}
R_1 & G_1 & B_1 & 0 & 0 & 0 & 0 & 0 & 0 \\
\vdots & \vdots & \vdots & \vdots & \vdots & \vdots & \vdots & \vdots & \vdots \\
R_M & G_M & B_M & 0 & 0 & 0 & \vdots & \vdots & \vdots \\
0 & 0 & 0 & R_1 & G_1 & B_1 & \vdots & \vdots & \vdots \\
\vdots & \vdots & \vdots & \vdots & \vdots & \vdots & \vdots & \vdots & \vdots \\
\vdots & \vdots & \vdots & R_M & G_M & B_M & 0 & 0 & 0 \\
\vdots & \vdots & \vdots & 0 & 0 & 0 & R_1 & G_1 & B_1 \\
\vdots & \vdots & \vdots & \vdots & \vdots & \vdots & \vdots & \vdots & \vdots \\
0 & 0 & 0 & 0 & 0 & 0 & R_M & G_M & B_M
\end{pmatrix}
\begin{pmatrix}
a_{11} \\ a_{21} \\ a_{31} \\ a_{12} \\ a_{22} \\ a_{32} \\ a_{13} \\ a_{23} \\ a_{33}
\end{pmatrix}
\approx
\begin{pmatrix}
X_1 \\ \vdots \\ X_M \\ Y_1 \\ \vdots \\ Y_M \\ Z_1 \\ \vdots \\ Z_M
\end{pmatrix}
\tag{A.3}
$$

The Least squares solution to Equation A.3 is solved with QR Factorization [17]. This is a factorization of a $m \times n$ matrix $\mathbf{A}$ into a $m \times n$ matrix $\mathbf{Q}$, with property $\mathbf{Q}^T\mathbf{Q} = \mathbf{I}$ ($\mathbf{Q}$ is orthonormal), and a $n \times n$ upper triangular matrix $\mathbf{R}$, i.e. $\mathbf{A} = \mathbf{QR}$. The matrices $\mathbf{Q}$ and $\mathbf{R}$ are calculated through a number of Householder Transformations [11]. The least squares solution to Equation A.1 is a minimization of $\|\mathbf{b} - \mathbf{Ax}\|_2^2$, where $\|\cdot\|_2$ is the length of a vector, also called the second norm of a vector. This expression be rewritten as:

$$\|\mathbf{b} - \mathbf{Ax}\|_2^2 = \|\mathbf{b} - \mathbf{QRx}\|_2^2 = \|\mathbf{Q}^T(\mathbf{b} - \mathbf{QRx})\|_2^2 = \|\mathbf{Q}^T\mathbf{b} - \mathbf{Rx}\|_2^2 \tag{A.4}$$

The third steps involes a multiplication with a matrix with orthonormal columns, i.e. $\|\mathbf{Q}^T\mathbf{x}\| = \|\mathbf{x}\|$. So, the solution to the least squares equation is:

$$\mathbf{x} = \mathbf{R}^{-1}\mathbf{Q}^T\mathbf{b} \tag{A.5}$$

One way to solve Equation A.5 in MATLAB is:

```
r=size(ptn,1);
A=ptn;
b=trg(:);

A2=[   A        zeros(r,3) zeros(r,3)
    zeros(r,3)    A        zeros(r,3)
    zeros(r,3) zeros(r,3)     A];


[Q R]=qr(A2);
[m n]=size(A2);
RN=R(1:n,:);
QT=Q';
QNT=QT(1:n,:);
x=inv(RN)*QNT*b;
```

where $x = (a_{11} \ldots a_{33})$ or directly by using MATLAB's \-command:

```
A=ptn;
b=trg;
X=A\b;
```

where $X = (a_{11} \ldots a_{33})$ is of size 3×3.

Appendix B

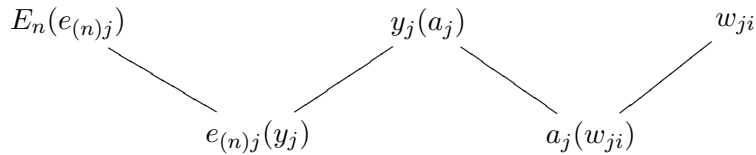# Calculation of the Jacobian matrix

The derivation of the Jacobian matrix in the modified back-propagation algorithm, see Table 3.2, is similar to the derivation of the error gradient in the school book back-progation algoritm [2], [10] with the exception of that the result of the former derivation evaluates the error on the individul output nodes, e_n, while the latter, Equation 3.9, evaluates the error of all added nodes, E_n.

$$
\mathbf{J} = \begin{pmatrix}
\frac{\partial e_1}{\partial w_1} & \frac{\partial e_1}{\partial w_2} & \cdots & \frac{\partial e_1}{\partial w_N} \\
\vdots & \vdots & \ddots & \vdots \\
\frac{\partial e_M}{\partial w_1} & \frac{\partial e_M}{\partial w_2} & \cdots & \frac{\partial e_M}{\partial w_N}
\end{pmatrix}
\tag{B.1}
$$

In Equation B.1, the number of rows M equals the number of training samples Q multiplied with the number of output nodes, and N is the total number of parameters, i.e. the weights and biases, in the network. It is the same size as $\mathbf{w}$ in Equation 3.7. In Equation B.1, the subscripts merly denotes the ordering, e.g. $\frac{\partial e_1}{\partial w_1}$ is the parital derivative of the first input sample on the first output node with respect to the first weight, which would be, according to the previously used notation in Table 3.1, $w_{11}^{(1)}$.

Error at output nodes

Now, we have to find the expression of the error on the output, starting with looking at the dependency relations of E_n, which are shown below. E_n is the summed error function over all output nodes in the nth sample and jth output node,

$$
\begin{array}{ccccc}
E_n(e_{(n)j}) & & y_j(a_j) & & w_{ji} \\
& \searrow & \nearrow \quad \searrow & & \nearrow \\
& e_{(n)j}(y_j) & & a_j(w_{ji}) &
\end{array}
$$

and we are interested in finding $\frac{\partial e_n}{\partial w_j}$. The above relation can be expressed with the chain rule as:

$$\frac{\partial E_n}{\partial w_{ij}} = \frac{\partial E_n}{\partial e_j} \frac{\partial e_j}{\partial y_j} \frac{\partial y_j}{\partial a_j} \frac{\partial a_j}{\partial w_{ij}}, \tag{B.2}$$

and by extracting the three right-most factors:

$$\frac{\partial e_j}{\partial w_{ij}} = \frac{\partial e_n}{\partial y_j} \frac{\partial y_j}{\partial a_j} \frac{\partial a_j}{\partial w_{ij}}, \tag{B.3}$$

we have aquired the desired expression. The next step is to calcluate each of the above factors starting from the left with differentiation of Equation B.4, which is the error in the jth output node,

$$e_{(n)j} = (t_{(n)j} - y_{(n)j}), \qquad \frac{\partial e_j}{\partial y_j} = -1 \tag{B.4}$$

and differentiating Equation B.5, which was previously given in Table 3.1.

$$y_j^{(l)} = \phi^{(l)}(a_j^{(l)}), \qquad \frac{\partial y_j}{\partial a_j} = \phi_j' \tag{B.5}$$

The last differeniation is made on Equation B.6. This Equation is same as Equation 3.5, apart from that the bias term is included in the sum.

$$a(\mathbf{y}) = \sum_{i=1}^{M} w_{ji} y_i, \qquad \frac{\partial a_j}{\partial w_{ij}} = y_i = \phi_i \tag{B.6}$$

Finally, we gather the above Equations into:

$$\frac{\partial e_j^{(L)}}{\partial w_{ij}} = -1 \phi_j' \phi_i, \tag{B.7}$$

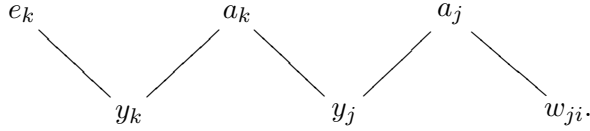which is the observed error on the output nodes.

Error in hidden nodes

The next step is to look at the error in the hidden nodes, where the error is back propagated from the output nodes. So, the error of jth node is dependent of the error from kth output nodes. This is expressed as:

$$e_{(n)j}^{(l)} = \sum_{k=1}^{K} e_{(n)k}^{(l+1)} \quad [\text{ or less cluttered}] \quad e_j = \sum_{k=1}^{K} e_k \tag{B.8}$$

for the nth sample. Differentiating Equation B.8 yields:

$$\frac{\partial e_j}{\partial w_{ij}} = \sum_{k=1}^{K} \frac{\partial e_k}{\partial w_{ij}} \tag{B.9}$$

Then, we look at the variables dependent of e_k,

$$
\begin{array}{ccccc}
e_k & & a_k & & a_j \\
& \searrow & & \nearrow \quad \searrow & & \nearrow \quad \searrow \\
& y_k & & y_j & & w_{ji}.
\end{array}
$$

Using the chain rule again, we are able find the parital derivative of e_k with respect to w_{ij},

$$\frac{\partial e_k}{\partial w_{ij}} = \frac{\partial e_k}{\partial y_k} \frac{\partial y_k}{\partial a_k} \frac{\partial a_k}{\partial y_j} \frac{\partial y_j}{\partial a_j} \frac{\partial a_j}{\partial w_{ij}} \tag{B.10}$$

The result of the derivation of Equation B.10 is the same as Equation B.7, with the exception of $\frac{\partial a_k}{\partial y_j}$ which is done in the following way:

$$a_k = \sum_{i=1}^{M} w_{kj} y_j, \qquad \frac{\partial a_k}{\partial y_j} = w_{kj} \tag{B.11}$$

Now, we evaluate each of the factors in B.10, using Equations B.4, B.5, B.11 , B.6 and B.9 yielding the following expresion:

$$\frac{\partial e_j}{\partial w_{ij}} = -1 \, \phi_j' \phi_i \sum_{k=1}^{K} \phi_k' w_{kj} \tag{B.12}$$